Finite element modeling (FEM) of porous additively manufactured ferromagnetic shape memory alloy using scanning electron micrograph (SEM) based geometries

by

Eric Myers

Submitted in Partial Fulfillment of the Requirements

for the Degree of

Master of Science in Engineering

in the

Mechanical Engineering

Program

YOUNGSTOWN STATE UNIVERSITY

May 2017

Finite element modeling (FEM) of porous additively manufactured ferromagnetic shape memory alloy using scanning electron micrograph (SEM) based geometries

Eric Myers

I hereby release this thesis to the public. I understand that this thesis will be made available from the OhioLINK ETD Center and the Maag Library Circulation Desk for public access. I also authorize the University or other individuals to make copies of this thesis as needed for scholarly research.

Signature:

Eric J. Myers, Student Date

Approvals:

Dr. C. Virgil Solomon, Thesis Advisor Date

Dr. Hazel Marie, Thesis Advisor Date

Dr. Daniel Suchora, Thesis Advisor Date

Dr. Salvatore A. Sanders, Dean of Graduate Studies Date

Abstract

The purpose of this research is develop an accurate modeling technique, using ANSYS software, to simulate the magneto-mechanical behavior of functional parts additively manufactured (AM) from Ni-Mn-Ga ferromagnetic shape memory alloy (FSMA) powders. Since bulk (100% dense material) Ni-Mn-Ga alloys are brittle, it is difficult to manufacture complex shaped parts from this material using typical machining methods. The technological interest in Ni-Mn-Ga resides on the large recoverable magnetic field induced strain (up to 10% in Ni-Mn-Ga single crystals). However, in the case of bulk polycrystalline Ni-Mn-Ga the magnetic field induced strain (MFIS) is much smaller, about 0.5%. Larger MFIS, up to 8%, was reported in Ni-Mn-Ga foam-like materials. In order to address the combined requirements of producing complex-shaped porous parts having high MFIS, binder jetting 3D printing has used to produce Ni-Mn-Ga parts showing reversible martensitic transformation. Compressive testing showed that AM parts do not share the mechanical properties of the bulk material. Their porosity makes the parts similar to a structure, so stress and strain distribution throughout the body is not uniform and theoretical stress and strain equations cannot be used. In addition, porosity weakens the parts due to the introduction of stress risers at the edges where particles are sintered together. To create a geometry that accurately captures the porous microstructure of a 3D printed Ni-Mn-Ga part, an initial micrograph of a polished cross-section of the part was recorded using a scanning electron microscope (SEM). Using Adobe Photoshop, the SEM micrograph was converted into a binary image to increase the contrast between the voids and the material. Thus, the border could be traced with polylines and converted into Drawing Exchange Format (DXF). This CAD data file format was then imported into

AutoCAD software, converted into a surface body, and imported into ANSYS Workbench software for modelling. Using FEA modeling it was possible to monitor the stress risers and to determine the fracture strain of the part. It was determined that at moderate stress-strain values the model can predict the mechanical behavior of the printed part. This thesis defense presentation will report on the current status of ANSYS simulation of mechanical behavior of porous Ni-Mn-Ga parts made by AM, and its feasibility as a useable modeling technique for porous functional parts made of shape memory alloys.

Acknowledgements

First I would like to thank my parents and my brother for their unending love and support. They have always served as great role models to me, and they instilled in me the drive and determination, without which, none of this would be possible.

I then would like to thank my advisor, Dr. C. Virgil Solomon, and the other members of my thesis committee, Dr. Hazel Marie and Dr. Daniel Suchora. They spent many hours reading and editing my thesis, but those hours pale in comparison to the six years they spent mentoring me throughout both my undergrad and graduated schooling.

I would like to give special thanks to Janet L. Gbur, Professor John Lewandowski, and his graduate students at Case Western Reserve University, as well as to Dr. Santo Padula, Dr. Othmane Benafan, Darrel Gaydosh, and Aaron Thompson at NASA Glenn Research Center. Without these people's time, knowledge, and resources, much of my research would not have been possible.

To my friends and the other members of my family, thank you all for the huge role in my life you play. Most of the time, grad school is just awful. You guys definitely made these last couple of years a whole lot more bearable.

To the graduate students at YSU, especially Matt Caputo, Rafaela Vannutelli, and Mike Juhasz, thank you for your assistance in my research.

Last I would like to thank Youngstown State University for use of its research facilities within the Center of Excellence in Material Science and Engineering.

Table of Contents

List of Figures

CHAPTER 1: INTRODUCTION

1.1 Definition of Shape Memory Alloys

Shape memory alloys (SMA) are a category of materials with the ability to return to a specific, predesigned shape after undergoing significant deformation induced by mechanical loading. External energy—thermal in the case of some alloys; magnetic in the case of others—is required. This process is known as the material's *shape memory effect*[1]. There are varieties of thermally activated SMAs, Cu-Al-Ni, Cu-Zn-Al, and Fe-Mn-Si to name a few[2], but the most widely studied is Ni-Ti. Commonly referred to as "nitinol", this alloy shows extraordinary shape memory effect, yet unlike many other thermal shape memory alloys is durable and capable of supporting a load. This makes it a prime candidate for SMA actuators, since the force its thermal actuation produces is capable of doing work comparable to electronic motors and pneumatic pistons. As with thermally activated SMAs, the are several magnetically activated SMAs, as well, including Ni-Mn-Ga, Fe-Pd, Fe-Pt, Fe-Ni-Co-Ti, Co-Ni-Ga, Ni-Mn-Al, and Co-Ni-Al. The focus of this thesis is on Ni-Mn-Ga. This alloy is preferable as it exhibits a higher field-induced strain than the other alloys[3].

1.2 Applications of SMAs

It is not difficult to envision industrial applications for the resistance of SMAs to plastic deformation. Anything that experiences fatigue, from eyeglasses frames to golf clubs, could benefit. The more interesting applications for SMAs are those relying on the controllability of the material's shape memory effect. In the bioengineering field, two widely used applications are stents and spinal spacers[4]. Both require being reduced in size to make insertion easier, but once deployed require mechanical stability at their designed sizes. In the case of thermally activated SMA, this is possible using a patient's own body temperature to maintain each device at the desired shape and size. The spinal spacer serves as an excellent shock absorber within a patient's spine as is can collapse with the vertebrae and expand repetitively to maintain its secure fit. The stent's design allows it to be flexible as to not tear the artery wall, yet its expansion also prevents it from getting dislodged so that it serves effectively to keep open where the artery has a plaque build-up. In addition to these bioengineering uses, SMAs also are becoming popular in the aeronautical industry. By controlling the heating and cooling of nitinol cables, lightweight actuators can be made to replace heavy motors and pneumatic pumps used for controlling the flaps of an airplane wing[5]. In the case of space exploration, instruments that need to be large in order to be effective, like satellite antennas or solar panels, pose a problem as room in a spacecraft is limited. SMAs allow these devices to be stowed much more compactly and can be easily deployed when needed[5]. For these applications, nitinol is most commonly used as it is the most rugged and reliable. However, the frequency at which nitinol and other thermally activated SMAs can be

actuated is a limiting factor in some cases. Because the material requires successive heating and cooling cycles, these SMAs typically can only cycle at about 10 Hz. Alternatively, magnetically activated SMAs, sometimes called ferromagnetic shape memory alloys (FSMAs), can achieve frequencies similar to piezoelectric materials[6]. Some studies show actuations frequencies of FSMAs as high as 2 kHz[7]. Ni-Mn-Ga is a FSMA capable of achieving the same order of strain as its thermally activated counterpart, but at a much quicker rate. This makes Ni-Mn-Ga more appealing for actuators used in applications like transducers, which are requiring high frequency bandwidths[8]. In addition to using such elements as actuators, FSMA can be used for sensors. The same magnetic properties that give these materials sensitivity to magnetic fields also give them variable deformation-dependent impedances, which can be measured and used to sense change in position[8].

1.3 Mechanism of Shape Memory Effect

1.3.1 Phases of Shape Memory Alloy

The unique abilities of shape memory alloys come from their crystalline structure. Twin boundaries within the material have different relaxed states depending on environmental conditions. When environmental conditions change, the boundaries twin or de-twin to orient the crystals into the new, appropriate relaxed state, or *phase*. The high-temperature phase is *austenite*. Austenite is the phase the crystal resides in when the temperature is above the austenitic activation temperature (T_{As}). The low-temperature phase is martensite. In the case of one way shape memory effect, if austenite is cooled below the martensitic transformation temperature (T_{Ms}), and no magnetic field is present, the austenitic phase will transform into the non-stressed martensite phase, due to diffusionless martensitic transformation. No macroscopic deformation is noticeable during direct martensitic transformation. When a mechanical stress is applied, de-twinning of the twinned martensitic phase occurs and the crystal accrues large deformation. For the deformed martensitic structure, the elastic potential energy is insufficient to return the martensite back into its unstressed state. The crystalline structure will remain in this state until it is heated or a magnetic field is applied, and the cycle will start all over.

It is worth noting that the driving force of phase change from de-twinned martensite to austenite in FSMA is not restricted to magnetism. Ferromagnetic shape memory alloys,

such as Ni-Mn-Ga, are also responsive to temperature. This becomes very important when trying to model FSMAs, as the interfacial friction within the material causes it to heat up as it cycles. This can significantly alter the predicted response of the FSMA to magnetism alone as will be explained in later sections. It is important to know both T_{As} and T_{Ms} for the particular alloy being used, as both have a strong compositional dependence. Another temperature worth noting is the Curie temperature, because above it, the FSMA becomes paramagnetic. This temperature (approximately 376 K for Ni-Mn-Ga alloys) shows only slight variation with changes in composition[9].

1.3.2 Variants

Austenite has a higher crystallographic symmetry than martensite. In the case of Ni-Mn-Ga, all of the atoms are located in the sites of a body-centered cubic lattice. Comparatively, martensite has either some form of tetragonal or orthorhombic structure. Because of this reduced symmetry, the crystals can have different orientations from one another also known as variants. For convenience of representation, the martensitic variants are usually simplified[9]. A common simplification is assuming only variants with magnetization directions parallel with the primary coordinates, Figure 1-1. The same simplification will be assumed in this thesis, but it is important to note, that SMAs can have as many as 192 possible variants in which their martensitic structure can reside[10].

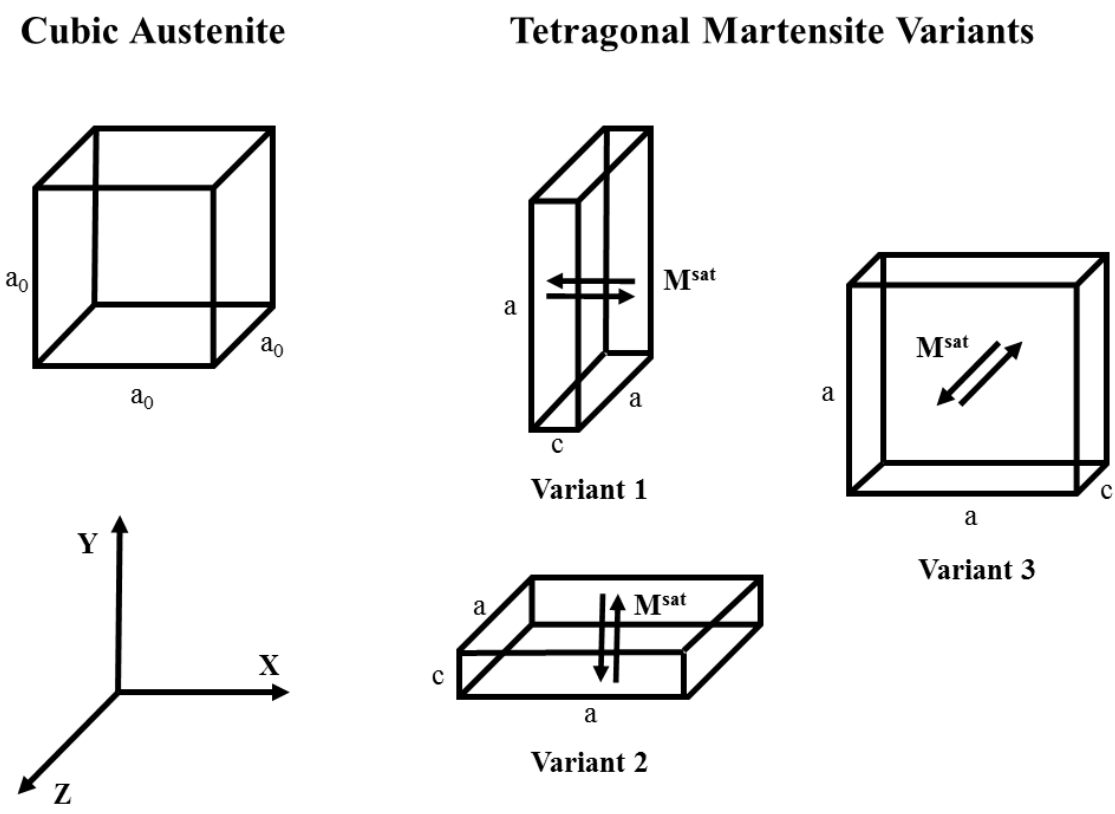

Figure 1 - 1: Crystal structures of the cubic austenite phase and the tetragonal martensite phases of Ni-Mn-Ga in its different orientations/variants. The arrows indicate both possible magnetization vector orientations along the magnetic easy axis of each variant.

The magnetic easy axis (*c*) refers to the crystallographic direction parallel (positive or negative) with the local magnetization vector of each variant. In the case of these tetragonal unit cells, *c* is the short edge. The local magnetization vector of each variant is the key to the shape memory effect of FSMAs, as this phenomenon is driven by their reorientation. In the presence of a sufficient external magnetic field, magnetic *domain wall motion* and the *magnetization vector rotation* are common in all ferromagnetic materials. In FSMAs, the rotation of the magnetization vector causes reorientation of the martensite variant.

To increase the responsiveness of the material further, an axial mechanical stress can be applied to polycrystalline FSMAs before applying the magnetic field. This reorients the two variants whose magnetic easy axes are perpendicular to the applied load[8]. With the applied stress favoring just one particular variant, there will be an even greater response to the external field as every crystal will experience vector rotation[9]. This is shown in Figure 1-2 as variant 1 (M1) and variant 3 (M3) are compressed into variant 2 (M2).

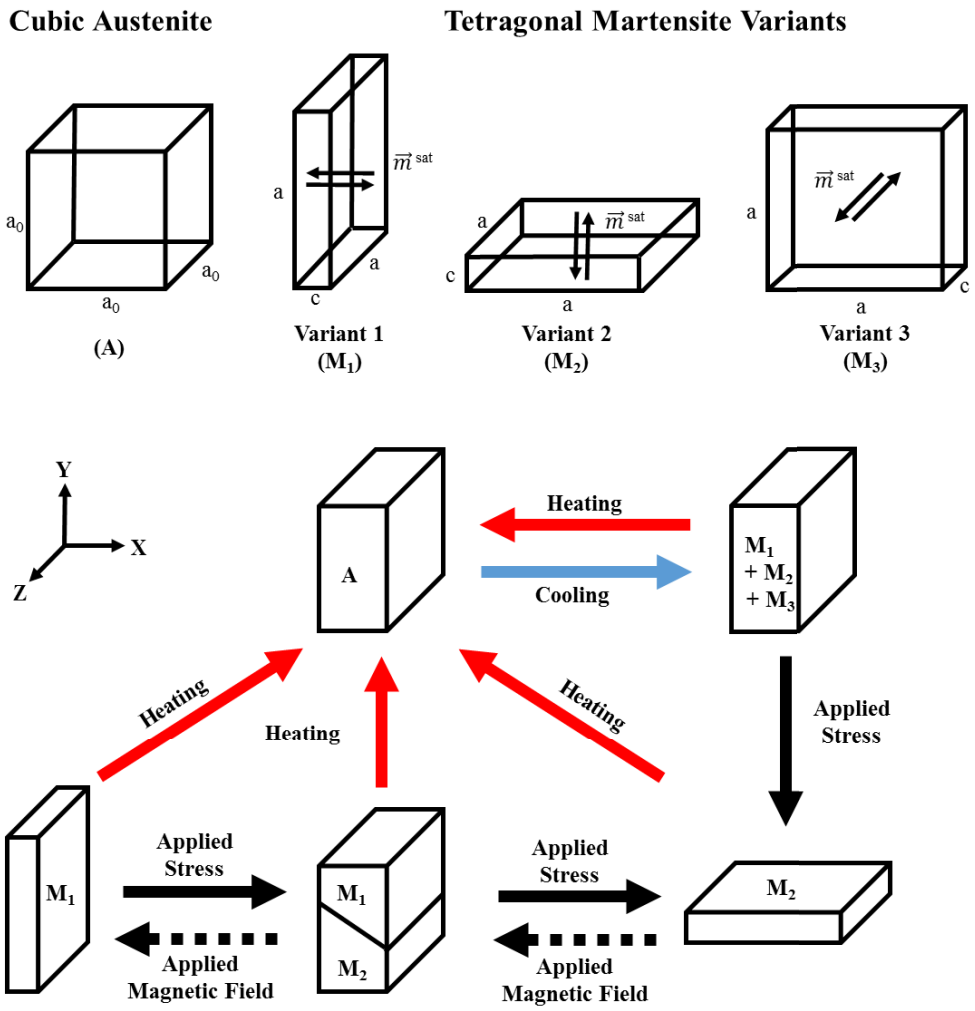

Figure 1 - 2: Effects of mechanical stress, magnetic field, and temperature of FSMA reorientation behavior.

As shown in Figure 1-2, by applying the stress along the y-axis, the favored variant becomes M2, while the other two are nearly eliminated. When the magnetic field is applied in the x-direction, M1 gradually begins to form creating nucleation sights. As the nucleation sights get larger, the rate at which M1 forms increases, then slows as the volume of M2 becomes less than that of M1. Because of this, there is a hysteresis response of the strain to the magnetic field[9]. This magnetic field-strain relationship is shown in Figure 1-3.

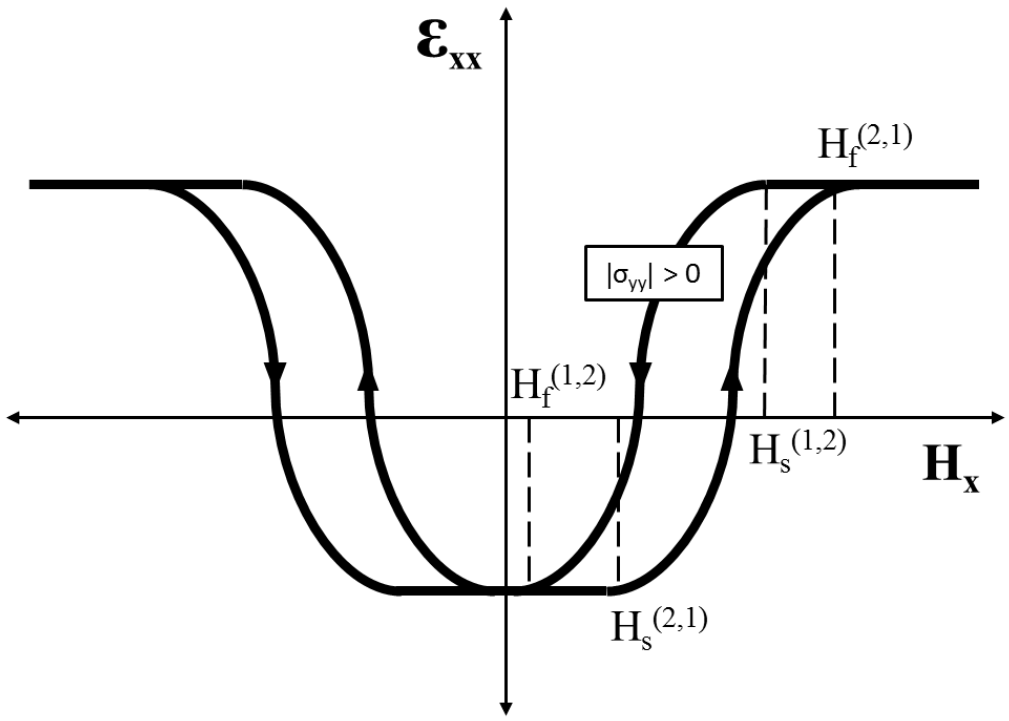

Figure 1 - 3: Strain-magnetic field response curves of FSMAs: $H_s^{(2,1)}$ is the start of variant shift from M2 to M1; $H_f^{(2,1)}$ shows the final product of total M1; $H_s^{(1,2)}$ and $H_f^{(1,2)}$ show the reverse products respectively.

Notice that the strain starts below zero due to the pre-stress applied to create the single variant state (M2).

1.4 Modeling Shape Memory Alloys

Shape memory alloys are being used commercially already as dampers and shock absorbers, as well as the stents and spinal spacers mentioned previously. However, these devices are limited as they can only make use of the material's fully recovered austenite phase. Any device requiring precision like a FSMA sensor or transducer needs to be highly predictable and therefore controllable when the austenite and martensite are in between full cycles. For this reason, many models have been proposed to aid the SMA's predictability. Because of its nonlinear behavior, modelling SMAs has proved to be a challenge for many researchers leading to a variety of proposed models. Three models will be discussed in the present work: the *micromechanical model*, the more modern *multi-mechanical based unified SMA material model*, and the more common *phenomenological model*. To better understand the complications of modelling SMAs, the ideal SMA stress-strain curve will be explained first.

1.4.1 Hysteresis Curve

The hysteresis—sometimes referred to as "flag-like"—stress-strain curve for the pseudoelastic response of SMAs under uniaxial loading is shown in Figure 1-4. It is worth noting that SMA's pseudoelastic behavior varies with temperature, so isothermal conditions must be considered for an idealized hysteresis curve.

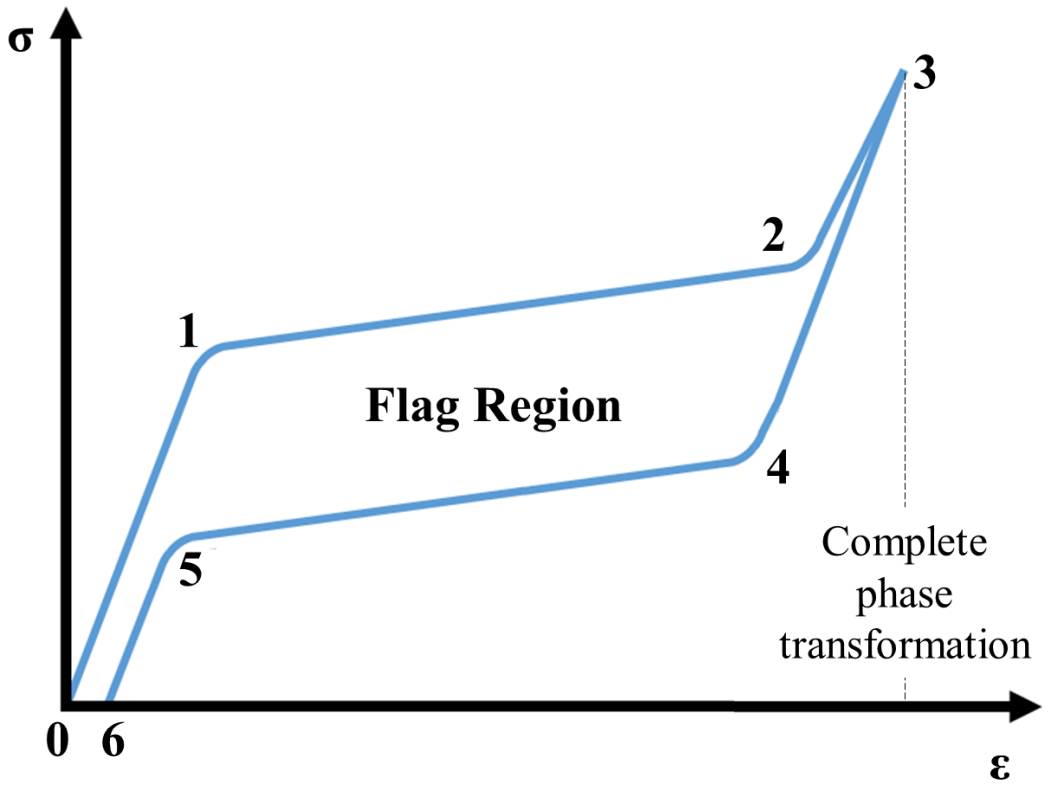

Figure 1 - 4: Ideal hysteresis stress-strain curve for pseudoelastic response of SMAs to uniaxial isothermal loading conditions.

This idealized behavior is a 1D representation of the flow stress of SMAs above T_{Af} or at saturation magnetization ($\vec{m}^{sat}$). At point 0, the SMA is in a zero stress austenitic phase. As a load is applied, the material exhibits purely elastic stress until its critical point, point 1, is reached. The region from point 1 to 2 is the forward phase transformation from austenite to martensite. This region experiences gradual hardening, which is relatively constant in ideal circumstances. From points 2-3, the rate of hardening becomes larger as the material reaches a purely martensitic phase (point 3). As the load is removed, the SMA again shows purely elastic behavior to point 4. Notice the critical stress that causes the martensite to austenite transition is less than the reverse. Points 4 and 5 correspond to the rapid reverse of 1 and 2, as the martensite begins its full transformation to austenite

(point 6). The offset of point 0 and 6 indicates the existence of retained martensite. Many models disregard this residual strain, but as the SMA cycles, its effect become too significant to ignore. Repeated thermo-magneto-mechanical loading induces permanent changes in the material's microstructure limiting recoverable transformation induced strains[12]. This can be caused by the formation of preferred variants, as mentioned in the previous section, and/or by slip dislocations just like in other metals. For this reason, "training" is usually required involving a thermo-magneto-mechanical cycling treatment to stabilize the material's response before it is usable with any amount of precision.

It is worth noting that though the stress-strain behavior displayed in Figure 1-4 is similar for SMAs in both tension and compression, they are not equal and opposite. This concept can be observed experimentally, but the reasoning for this is not yet confirmed[11].

1.4.2 Micromechanical Model

The micromechanical model is not as common as the other two, but it has proved to be quite accurate at repeating experimental results. First, extensive experimental data is required to find the exact crystallography of both the martensitic and austenitic phases. Knowing this, the translational motion of the single crystalline plane can be deduced and represented by a reorientation matrix. In the case of single crystal SMAs, this microscopic motion would then be scaled proportionately to describe the material's macroscopic deformation. However, in polycrystalline SMA, each grain resembles a separate habit plain which can be in hundreds of orientations. The more grain

orientations the user tries to represent, the more numerous the reorientation equations become, and the more computing power required. Averaging techniques are typically used to condense the number of habit planes, but calculations can still be excessive. Volumetric ratios of austenite and martensitic variants are assumed based on experimental results for the SMAs transformation temperatures and stress-strain behavior, then based on thermodynamic work-energy equations, the transformation equation of the macroscale model is determined.

As mentioned, these models are good at recreating experimental results, but they are limited to the particular alloy for which they were designed and cannot be used independently. Creating the rotation matrices requires a large number of internal variables derived from extensive experimentation, so required computing power is another of this model's flaws. Also, these equations demand that the load conditions are kept the same, and the SMA is cycled slow enough as to not accrue any permanent strain. Any disruption to the volumetric ratios of austenite and the martensitic variants can cause the model's structure to break down[12].

1.4.3 Multi-mechanical based unified SMA material model

The multi-mechanical based unified SMA material model is one of the most unique models to date. Unlike most theoretical SMA models which are rate independent and useful for describing the behavior of only a specific alloy in one direction, the unified SMA material model is designed to be universally applicable to all SMAs, as well as

multiaxial and rate dependent. This model is produced by dividing a part into a finite number of elements to study their solid mechanic behavior individually, then combining these behaviors to describe the overall behavior of the part. This model is ideal for FEA software packages like ABAQUS, ANSYS, and LSDYNA, which can utilize the framework equations most effectively eliminating the need of the user to treat the force and energy distribution across the model as homogeneous. These framework equations consist of a strain energy equation based on Gibb's free energy and a dissipation function based on a generalized potential-based viscoelastoplasticity model that incorporates direction specific stress tensors and adaptive kinematic hardening variables. The properties of SMAs are rate dependent. It is not known whether this is due to the viscoplasticity of the material or its internal latent heat generation and absorption, but it is certain that rate dependency is needed for an accurate model. To accommodate this, the viscoelastoplasticity model's adaptive hardening variables use the rate at which the model transitions between any two consecutive stages of the six shown in Figure 1-4 to manipulate the remaining hardening functions which correspond to the transitioning between each of the other pairs of consecutive stages. This model is quite capable of predicting the evolutionary response of SMA, regardless of their composition, but it is still slightly limited, however, relying on the total deformation being "small" (less than the elastic limit)[12].

1.4.4 Phenomenological Model

The phenomenological model is the most predominant in literature. Instead of relying on the complexities of the micro-scale reorientation matrix like the micromechanical model,

this model uses macroscopic reorientation functions based on classical plasticity equations to track the pseudoelastic stress-strain mechanics of the material (see Figure 1-4). Additionally it implements the second law of thermodynamics to account for the free energy potential within the body to predict a reorientation function which represents the materials shape memory effect. Both of these things makes the phenomenological model easy to adapt and implement to any SMA, which is a major reason for its wide spread use. A disadvantage to this model, like the micromechanical modal, is it relies heavily on a level of certainty of the volumetric ratios of austenite and the various martensitic variants. This is not as much of an issue if 1D uniaxial loading is assumed, but for a 3D multiaxial problem, it is inevitable that variants will form in varying orientations disrupting the volumetric ratios. Another disadvantage comes from the two separate sets of driving equations that typically must be implemented on the model to accurately predict the SMA's differing tension-to-compression behavior. This asymmetry presents convergence issues in many models. The most critical issue with these models is they usually assume the material is isotropic, and by overlaying the classical plasticity functions over experimental uniaxial stress-strain data, a 3D model is based off the isotropic material. Because this is untrue, the model cannot truly be adaptive; meaning if the model is run in any way differing from how the experimental conditions were derived, the results will have little accuracy. This is part of the reason for these models' inability to simultaneously model both superelasticity and shape memory effect[12]. This being said, the adaptability of this type of model leaves it open to research and improvement as the multi-mechanical based unified SMA material model shows. The

computational strategy used by ANSYS are based primarily on the works of Auricchio *et al*.[13, 12] and are shown in detail in the following section.

1.4.5 The Constitute Model for Shape Memory Alloys used by ANSYS

As mentioned before, the phenomenological model assumes isotropy of the material, which ultimately limits the model to the experimental loading conditions from which the material properties were derived. However, for the purpose of this work, the accuracy this type of model has shown replicating experimental data is sufficient. Also as mentioned, an assumption is made regarding the composition of the variant phases within the material[13].

$$\xi_A + \xi_M = 1 \tag{1.1}$$

In this case, ξ_A is the volume fraction of the austenite phase and ξ_M is the volume fraction of the martensite phase. This model assumes the Drucker-Prager Loading function, F, as follows.

$$F = q + 3\alpha p \tag{1.2}$$

Where, q is the effective stress tensor of the material, α differentiates the material's response depending if it is in tension or compression, and p is the hydrostatic (or volumetric) stress. Because this model assumes isotropy, deviatoric stress, s, is often used. So, the following is true.

$$\sigma = \begin{bmatrix} \sigma_{11} & \sigma_{12} & \sigma_{13} \\ \sigma_{21} & \sigma_{22} & \sigma_{23} \\ \sigma_{31} & \sigma_{32} & \sigma_{33} \end{bmatrix} \tag{1.3}$$

$$\sigma_{Hydrostatic} = p = \frac{\sigma_{11}+\sigma_{22}+\sigma_{33}}{3} = \frac{\sigma}{3} \tag{1.4}$$

$$s = \sigma - p \cdot I = \begin{bmatrix} \sigma_{11} - p & \sigma_{12} & \sigma_{13} \\ \sigma_{21} & \sigma_{22} - p & \sigma_{23} \\ \sigma_{31} & \sigma_{32} & \sigma_{33} - p \end{bmatrix} \tag{1.5}$$

In this case, *I* is the identity tensor.

$$q = \sqrt{\frac{3}{2} s : s} \tag{1.6}$$

The asymmetry of the tension-compression response of the material require the following modifier.

$$\alpha = \frac{\sigma_c^{AM} - \sigma_t^{AM}}{\sigma_c^{AM} + \sigma_t^{AM}} \tag{1.7}$$

The material parameters used come from the idealized stress-strain diagram of superelastic behavior, shown in Figure 1-5.

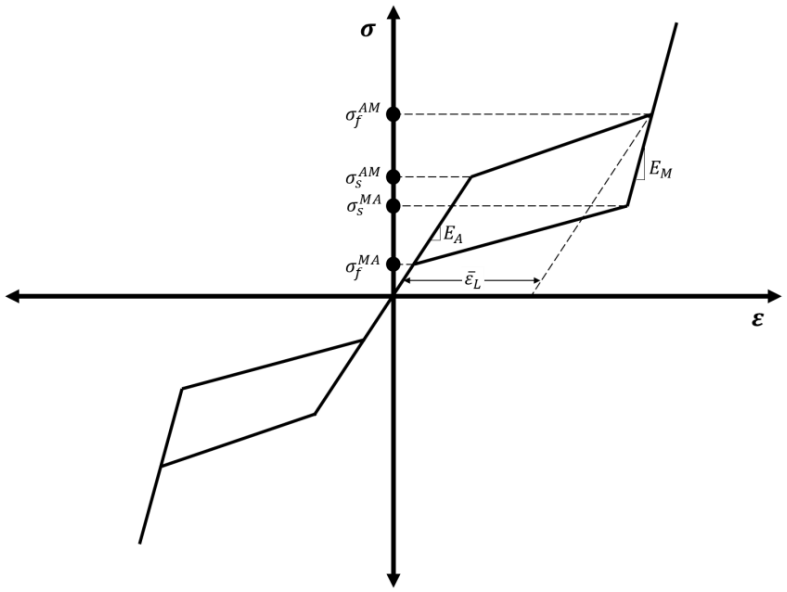

Figure 1 - 5: Idealized stress-strain diagram of superelastic behavior.

Figure 1-5 also shows E_A and E_M, the elastic moduli of the austenitic phase and the martensitic phase respectively, as well as $\bar{\varepsilon}_L$, the maximum residual strain. The model is limited to the domain of the experimental data. Therefore, elastic domain radii, R, are determined.

$$R_f^{AM} = \sigma_f^{AM}(1+\alpha) \tag{1.8}$$

$$R_s^{AM} = \sigma_s^{AM}(1+\alpha)$$

$$R_f^{MA} = \sigma_f^{MA}(1+\alpha)$$

$$R_s^{MA} = \sigma_s^{MA}(1+\alpha)$$

These radii are then used to control the evolution of the martensite volume fraction ($\dot{\xi}_M$).

$$H^{AM} = \begin{cases} 1\ if, & \begin{cases} R_s^{AM} < F < R_f^{AM} \\ \dot{F} > 0 \end{cases} \\ 0\ if\ , & otherwise \end{cases} \tag{1.9}$$

$$H^{MA} = \begin{cases} 1\ if, & \begin{cases} R_f^{MA} < F < R_s^{MA} \\ \dot{F} < 0 \end{cases} \\ 0\ if, & otherwise \end{cases}$$

$$\dot{\xi}_M = \begin{cases} -H^{AM}(1-\xi_M)\left(\frac{\dot{F}}{F-R_f^{AM}}\right), & A \to M\ Transformation \\ H^{MA}\cdot\xi_M\left(\frac{\dot{F}}{F-R_f^{MA}}\right) & , \ M \to A\ Transformation \end{cases} \tag{1.10}$$

With $\dot{\xi}_M$ defined, superelastic stress-strain relation is then defined as follows:

$$\sigma = D:(\varepsilon - \varepsilon_{tr}) = \frac{\partial W}{\partial \varepsilon} \tag{1.11}$$

$$\dot{\varepsilon}_{tr} = \dot{\xi}_M \bar{\varepsilon}_L \frac{\partial F}{\partial \sigma} \tag{1.12}$$

In this case, D is the elastic stiffness tensor, which takes deviatoric stresses into account, and W is the energy of the material. As mentioned before, ψ is the driving equation for

phenomenological models. In the case of this model, the free energy potential is assumed using linear relations of the ideal stress-strain relationships.

$$\psi(\varepsilon, T, \varepsilon_{tr}) = \left[\frac{1}{2}(\varepsilon - \varepsilon_{tr})D:(\varepsilon - \varepsilon_{tr})\right] + \left[\frac{1}{2}h\|e_{tr}\|^2\right] + [\tau(T)\|e_{tr}\|] + \left[I_{\bar{\varepsilon}_L}(e_{tr})\right] \quad (1.13)$$

$$\psi(\varepsilon, T, \varepsilon_{tr}) = [\psi_E] + [\psi_H] + [\psi_T] + \left[I_{\bar{\varepsilon}_L}(e_{tr})\right]$$

In the above equation, ε is the total strain, ε_{tr} is the total transformation strain, e_{tr} is the deviatoric transformation strain, τ is a positive and monotonically increasing temperature function, T is temperature, h is the material hardening parameter, and $I_{\bar{\varepsilon}_L}$ an indicator function associated to the transformation strain.

$$I_{\bar{\varepsilon}_L}(e_{tr}) = \begin{cases} 0 & if\ 0 \le e_{tr} \le \bar{\varepsilon}_L \\ \infty & if\ otherwise \end{cases} \quad (1.14)$$

This function is required as the model is only defined to $\bar{\varepsilon}_L$ and must be terminated beyond this limit. The free energy from the elastic stiffness and hardening during the phase transformation is illustrated in Figure 1-6.

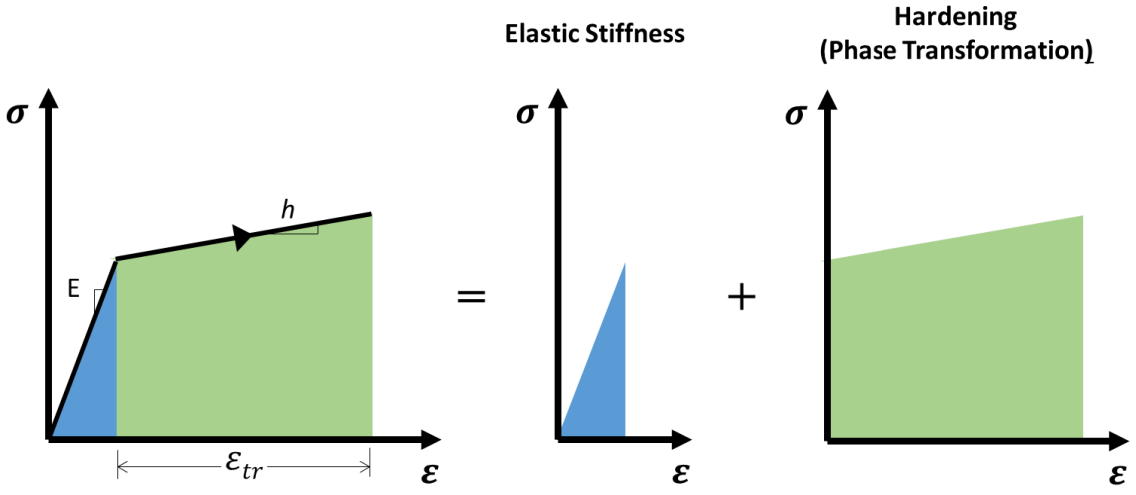

Figure 1 - 6: Energy density from elastic stiffness and hardening.

It is known the area under a stress-strain curve is the "energy density" or the amount of energy per unit volume. Therefore, the following is known about the elastic stiffness, hardening, and temperature functions.

Elastic Stiffness Function:

$$\psi_E = Area \approx \int_0^{\varepsilon-\varepsilon_{tr}} (E\varepsilon)\, d\varepsilon = \frac{1}{2}(\varepsilon - \varepsilon_{tr})\sigma \tag{1.15}$$

To take deviatoric stresses into account, D is substituted for σ.

$$\sigma = D\colon(\varepsilon - \varepsilon_{tr}) \tag{1.16}$$

To account for the material's change in stiffness when its phase changes, the following correction is needed.

$$D = \frac{\|e_{tr}\|}{\bar{\varepsilon}_L}(D_M - D_A) + D_A \tag{1.17}$$

This assumes the Poisson's ratio of A and M are the same.

$$\psi_E = \frac{1}{2}(\varepsilon - \varepsilon_{tr})\, D\colon(\varepsilon - \varepsilon_{tr}) \tag{1.18}$$

Hardening Function:

$$Area = \int_0^{\varepsilon_{tr}} (h\varepsilon)\, d\varepsilon = \frac{1}{2} h {\varepsilon_{tr}}^2 \tag{1.19}$$

Because of the changing of the crystalline structure's geometry during the transformation phase, the magnitude of the deviatoric strain is substituted in for ε_{tr}.

$$\psi_H = \frac{1}{2} h \|e_{tr}\|^2 \tag{1.20}$$

Temperature Function:

The temperature equation, *τ(T)* comes from the graph shown in Figure 1-7.

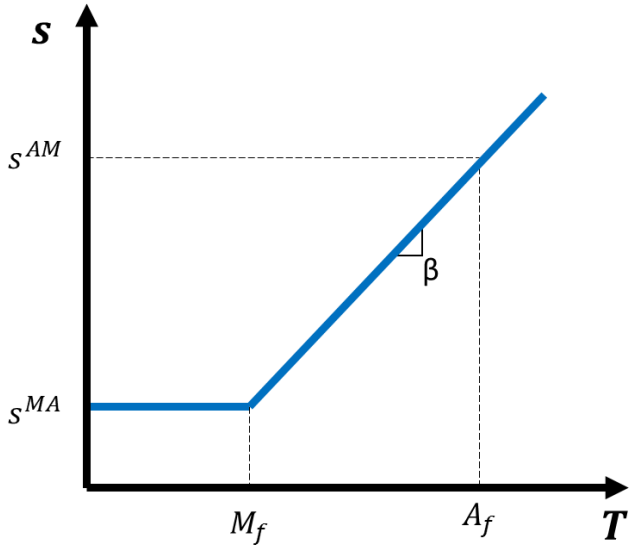

Figure 1 - 7: Relationship between deviatoric stress and transformation temperature[1].

$$\tau(T) = \beta(T - M_f) \tag{1.21}$$

$$\psi_H = \tau(T)\|e_{tr}\| \tag{1.22}$$

In this equation, β is the material parameter related to the dependence of stress inducing transformation. Notice it is related to the deviatoric stress of the system. The total stress in the system can then be shown as follows.

$$\sigma = \frac{\partial \psi}{\partial \varepsilon} \tag{1.23}$$

Specifically, the transformation stress is denoted as follows.

$$X_{tr} \in -\frac{\partial \psi}{\partial e_{tr}} \tag{1.24}$$

$$X_{tr} = s - [\tau(T) + h\|e_{tr}\| + \gamma]\frac{e_{tr}}{\|e_{tr}\|} \tag{1.25}$$

Where γ is just a subdifferential of the indicator function $I_{\bar{\varepsilon}_L}(e_{tr})$, which alerts the model when it has reached the limits of its dom ain.

$$\gamma = f(x) = \begin{cases} 0, \ 0 < e_{tr} < \bar{\varepsilon}_L \\ \geq 0, \ \|e_{tr}\| = \bar{\varepsilon}_L \end{cases} \tag{1.26}$$

The last note is how this model handles the tension-compress asymmetry of the material. In this case, a Prager-Lode type limit surface is assumed which incorporates the following functions:

$$F(X_{tr}) = \sqrt{2J_2} + m\frac{J_3}{J_2} - R \tag{1.27}$$

Where:

$$J_2 = \frac{1}{2}(X_{tr}^2 : 1) \tag{1.28}$$

$$J_3 = \frac{1}{3}(X_{tr}^3 : 1)$$

$$m = \sqrt{\frac{8}{3}}\frac{\sigma_c \sigma_t}{\sigma_c + \sigma_t}$$

In conclusion, the primary driving equations are 1.12, 1.13, and 1.23.

1.4.6 Microscale Image-Based Finite Element Modeling

This finite element model was based off an idea used by WHEMCO Inc. to improve the lifespan of the rolls used in their hot strip rolling mill[14]. The WHEMCO team got their idea from a software developed by National Institute of Standards and Technology: Object-Oriented Finite Elements (OOF) – Finite Element Analysis of Microstructures[15]. The high speed steel (HSS) shell of the work roll (WR) and the backup roll (BUR) are

subjected to extreme mill loading and environmental conditions and succumb to wear and thermal fatigue over time. The mechanical properties of the shell of the work roll vary radially based on the volume fraction of the alloying elements, morphology, crystalline structure, and the radial distribution of carbides within the matrix, so the shell cannot be modeled as homogeneous. Crack propagation tends to occur in the shell of the work roll near the surface of the roll's carbide-matrix interface, so a model that could be used to determine ideal rolling procedures, loading conditions, and environmental conditions was created. They used scanning electron microscope (SEM) micrographs of the HSS material and converted them into FEA models. X-ray energy dispersive spectroscopy (XEDS) was also used to differentiate the micro constituents within each micrograph and measure their composition. In order to import a SEM micrograph into FEA software, the micrograph was first converted to a raster, then into a vectored format which was imported into a CAD package. The CAD image was then imported into ANSYS Workbench where differing mechanical properties were assigned to the system, and mechanical as well as thermal loads could be applied[13].

1.5 Purpose

Poly-crystalline Ni-Mn-Ga shows significantly less magnetic field induced strain (MFIS) than single-crystalline Ni-Mn-Ga, 0.5% versus 10%, respectively[16,17]. This is due to the constriction caused by the grain boundaries within the structure which reduces twin boundary motion, which is responsible for magnetic shape memory effect[18]. Though this seems to make single-crystalline Ni-Mn-Ga the obvious choice for engineering applications, single-crystalline Ni-Mn-Ga is far less durable restricting its usefulness[19]. Moreover, Ni- Mn-Ga-based alloys are very brittle, therefore machining is nearly impossible. It is known that the MFIS can be increased in FSMA by increasing the porosity through synthesis of Ni-Mn-Ga foams. This helps eliminate some of the grain boundaries' constrains on twin boundary motion. A 8% MFIS was reported in Ni-Mn-Ga foams[20]. It is also known that the performance of magnetic materials are dependent on geometry as much as on the material properties[21]. The complex requirements of intricate-shaped porous parts made from Ni-Mn-Ga alloys, might be addressed by using additive manufacturing techniques. Binder jetting 3D printing of complex shaped Ni-Mn-Ga parts showing reversible martensitic transformation was first reported by an YSU team[22]. As mentioned previously, there are many proposed models of SMAs, however, no numerical modeling was reported on additively manufactured SMAs. The purpose of this research is to discover possible means of accurately modeling additively manufactured FSMA, and to predict the mechanical and memory properties of parts 3D printed from Ni-Mn-Ga ferromagnetic shape memory alloy powders. The method used will be similar to the microscale image-based finite element modeling proposed by WHEMCO Inc.

CHAPTER 2: EXPERIMENTAL METHODS

2.1 Sample Preparation for Compression Testing

In this work, Ni-Mn-Ga samples made using two different manufacturing methods were investigated: bulk, or 100% dense samples, and additive manufactured (AM) samples. Pure (99.99%) nickel, manganese, and gallium elements were arc melted together to prepare 49.73 at% Ni - 29.03 at% Mn - 21.24 at% Ga ingots. The ingots were then encapsulated in a quartz tubes filled with argon gas for the chemical homogenizing heat treatment, which was done at 1273 K for 24 hours. The cubic-shaped (5 mm x 5 mm x 5 mm) bulk Ni-Mn-Ga samples for compression testing were prepared from the ingots by sectioning, using Buehler IsoMet 1000 precision cutter. Other ingots were ball milled for 2 hours in order to obtain fine Ni-Mn-Ga metal powders. The powder was used in additive manufacturing of Ni-Mn-Ga samples for mechanical testing. The additive manufacturing method employed in this work was binder-jetting in ExOne X1-Lab 3-D printer. After printing, the parts were cured at 463 K for 4 hours. The cured parts were sealed in quartz tubes filled with an argon gas and sintered at 1275 K for 20 hours[22, 23]. Figure 2-1 shows bulk and AM Ni-Mn-Ga samples used for compression testing.

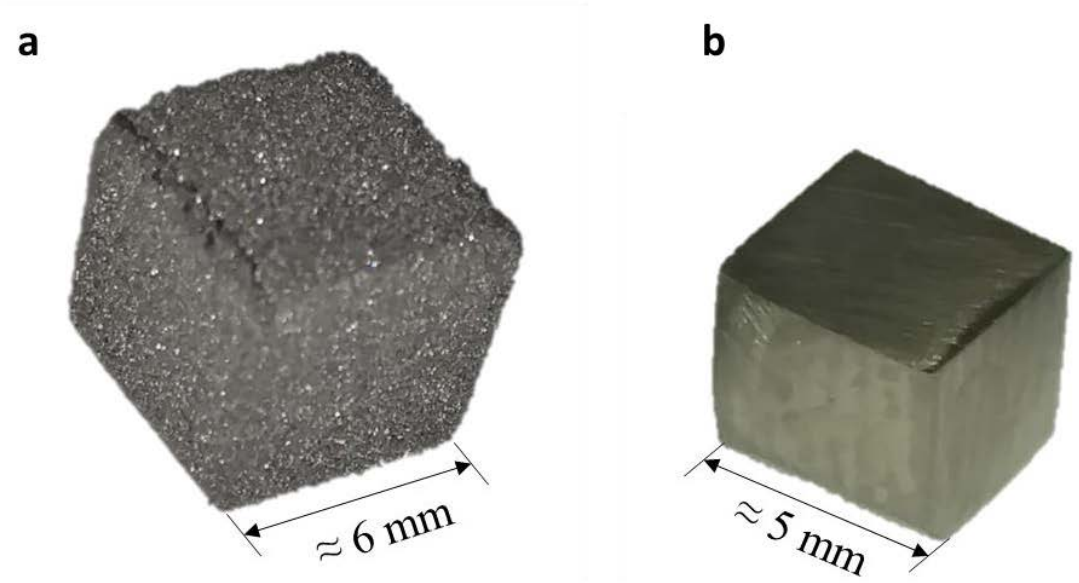

Figure 2 - 1: Compression test samples: (a) 3D printed Ni-Mn-Ga sample prepared by AM for mechanical testing; (b) Cubic-shaped bulk Ni-Mn-Ga sample.

2.2 Morphological and chemical investigation of 3D printed Ni-Mn-Ga samples

Morphological and chemical investigation of the samples was performed by scanning electron microscopy (SEM) and X-ray energy dispersive spectroscopy (XEDS). The electron microscopy investigation was performed in a JEOL JSM7600F Scanning Electron Microscope equipped with EDAX Octane Plus X-ray Energy Dispersive Spectrometer. Cross-sectional samples for SEM and XEDS analysis were prepared by sectioning, using the Buehler IsoMet 1000 precision cutter, followed by grinding and polishing until a mirror-like surface was obtained. Figure 2-2 (a) and (b) show electron micrographs recorded from the cross-sectioned surface of AM Ni-Mn-Ga samples. The part is not fully dense, and the porosity is clearly seen in the mirographs. The XEDS

spectrum in Figure 2-2 (c) confirms Ni, Mn, and Ga as constitutive elements of the 3D printed sample.

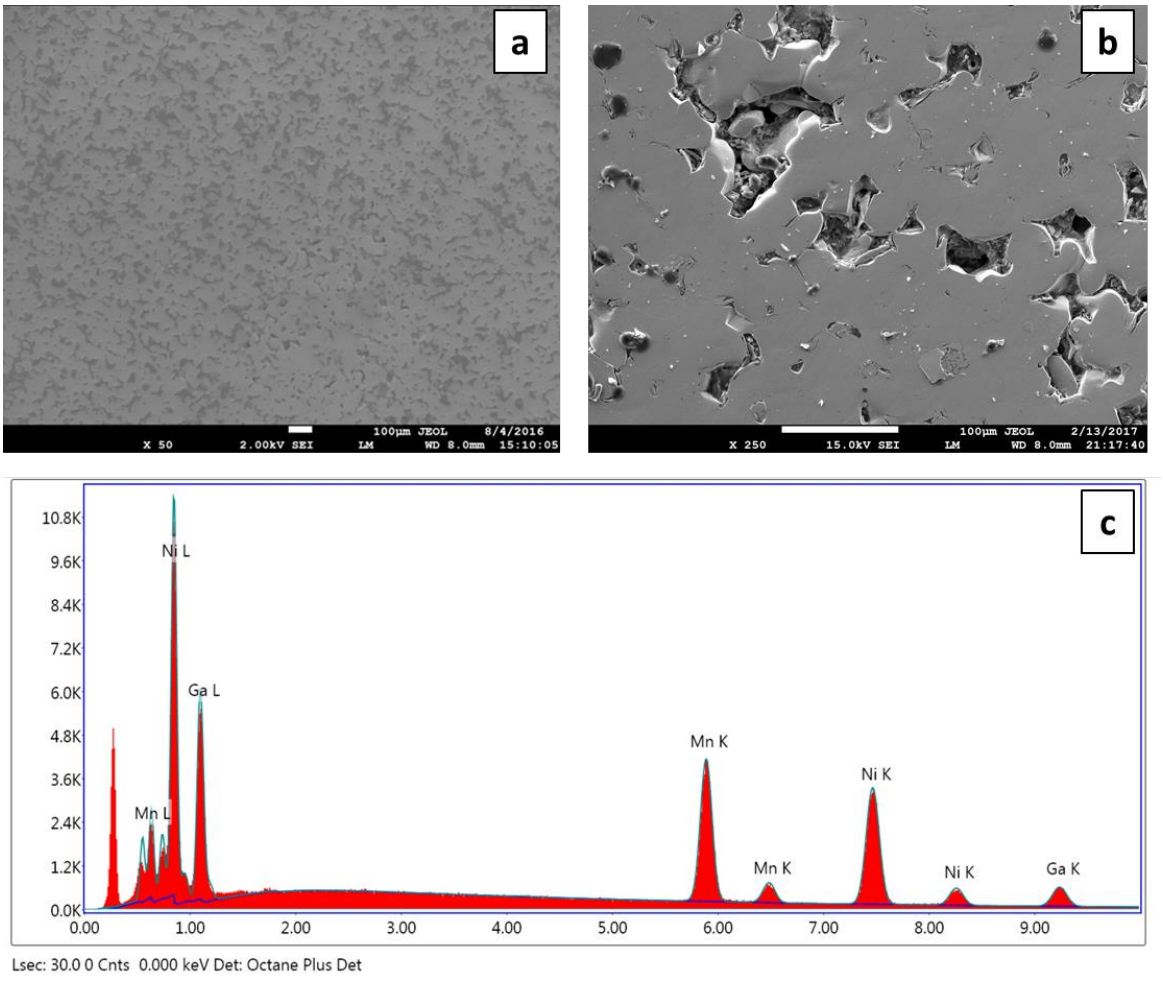

Figure 2 - 2: Morphological and chemical investigation of 3D printed Ni-Mn-Ga samples: (a) Secondary electron micrograph of cross-sectioned Ni-Mn-Ga sintered part; (b) Higher magnification secondary electron micrograph recorded from cross-sectioned sample; (c) XEDS spectrum from the sample in (a) indicating the sample's chemical constituents.

2.3 Mechanical properties measurement

In order to determine the mechanical properties of both bulk and AM Ni-Mn-Ga, uniaxial compression tests were performed using an Instron testing system. Due to a series of complications and limitations, some approximations were necessary in regards to the data acquired. One limitation was the sizes of both the bulk and AM samples used in the experiments. Several limiting factors determined the sample shape and dimensions: Ni-Mn-Ga ingot size, the amount of Ni-Mn-Ga powder available for printing, and the size limitation of the vacuum system. For example, the samples could only be as large as the inner diameter (10 mm) of the quartz tubes used in the chemical homogenization and sintering processes, and the quartz tubes used were specific to the vacuum system that was available. This is an issue because the goal of the experimental tests was to determine mechanical properties of the bulk and AM Ni-Mn-Ga. This means the length of the ideal test sample in the loading direction should be of an order at least twice the characteristic length (lateral dimensions) of the sample in order to ensure uniform load distribution at its center. This is in accordance to Saint-Venant's Principle[24]. The strain then should be measured at the sample's center. Adding even more difficulty to this issue, limited by what equipment was available, cutting and polishing of the test samples was done by hand, so no two samples were entirely identical despite best efforts. Therefore, it is expected that the top and bottom contact surfaces of the sample were not completely parallel. This introduces stress risers that lead to additional non-uniformity of load distributions within the samples. For these reasons, traditional engineering stress and strain equations used for axial loading ($\sigma = F/A$ and $\varepsilon = \Delta L/L_0$) are not entirely accurate

for the given samples. Also, due to the small size of the samples, traditional strain gages could not be used in acquiring experimental data as none could be found that were small enough and accurate at measuring large strains corresponding to the eventual superelastic behavior of Ni-Mn-Ga samples. Given these limitations, it was determined that the best means of acquiring accurate strain measurements was to use Digital Image Correlation (DIC) techniques[25]. By using DIC techniques accurate strain measurement is not affected by sample size. Access to these instruments was not readily available, so the number of test samples was limited. However, the data acquired showed significant enough trends that it was deemed sufficient for the purpose of this work.

2.3.1 Digital Image Correlation

Two different instruments were used for measuring strain in the test samples: an Arion 1-D axial non-contact extensometer from UVID Enterprises, LLC, available at Case Western Reserve University; and an ARAMIS system available at NASA Glenn. Both devices use high speed, high resolution cameras to track the change in position of points on the surface of a given sample. Paint is typically used to create higher contrast from the points being tracked and the rest of the surface of the sample.

The Arion 1-D axial non-contact extensometer (denoted UVID from now on) is shown in Figure 2-3[26]. The system consist of a high speed CCD camera and two illumination sources installed in the front of the mechanical testing instrument.

Figure 2 - 3: UVID non-contact extensometer.

To use this system, three fiduciary dots are painted on sample, as shown in Figure 2-4. This instrument utilizes a single camera with a polarized lens that further increase the contrast between the surface of the sample and the bright colored paint. The single camera limits the instrument to 1D and 2D measurements, but calibrating the instrument is easy since only the one camera requires focusing. Since the test was uniaxial and no longitudinal, transversal, or shear measurement had being taken, this instrument could be used with reliable accuracy.

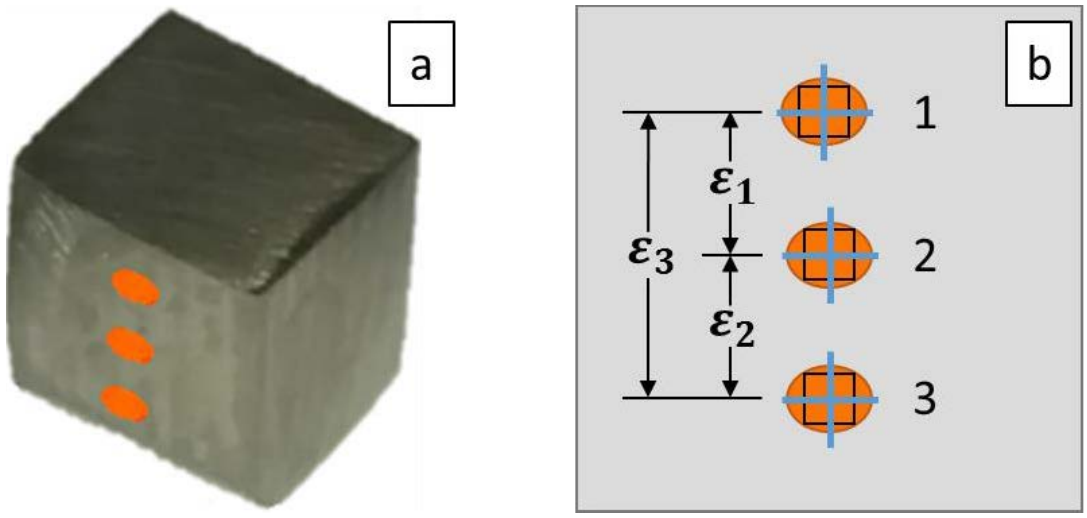

Figure 2 - 4: UVID System: (a) Bulk Ni-Mn-Ga sample showing the three fiduciary points; (b) Fiduciary map.

Using the polar decomposition theorem, the principal stretches of the fiduciaries are converted in real time into three strains (ε_1 from point 1 to 2, ε_2 from point 2 to 3, and ε_3 from point 1 to 3) by use of the Cauchy infinitesimal, Lagrangian and Hencky (logarithmic) strain formulation[26]. The polar decomposition theorem will be described in detail in section 2.3.2.

Figure 2-5 shows the ARAMIS system.

Figure 2 - 5: ARAMIS system.

This system utilizes two cameras providing full 3D strain and displacement measurements. A calibration panel is required to bring both of the cameras into focus on the measuring range appropriate to the sample[27]. These calibration panels are shown in Figure 2-6.

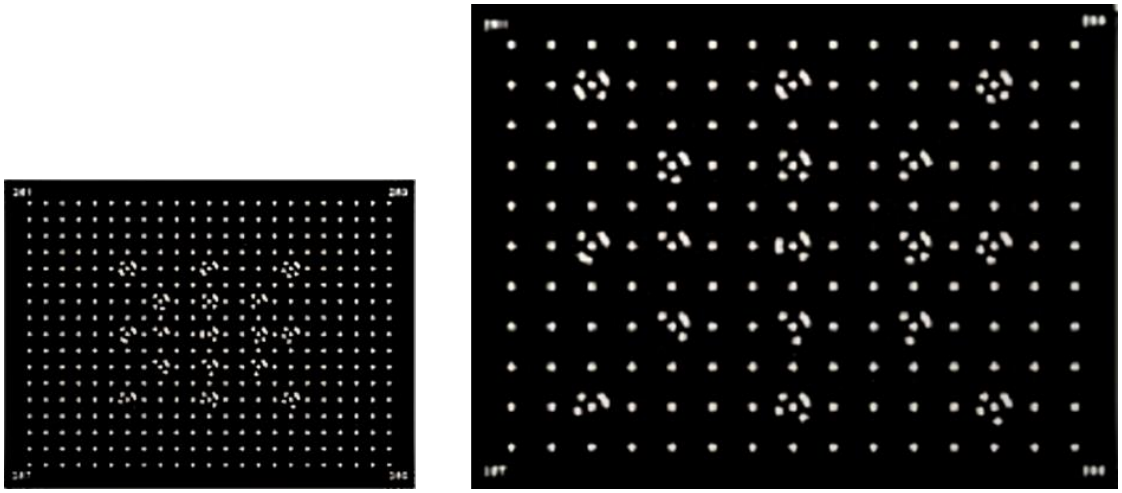

Figure 2 - 6: Calibration panels for Aramis system.

The surface of each sample being measured was first painted white. Black paint was then speckled onto the surface to create features of high contrast that the cameras could better track. The ARAMIS software then overlays a grid on top of the surface and assigns a global coordinate system. The grid divides the surface into a series of individual subsets with specific dimensions and coordinates relative to the origin of the global coordinate system, Figure 2-7.

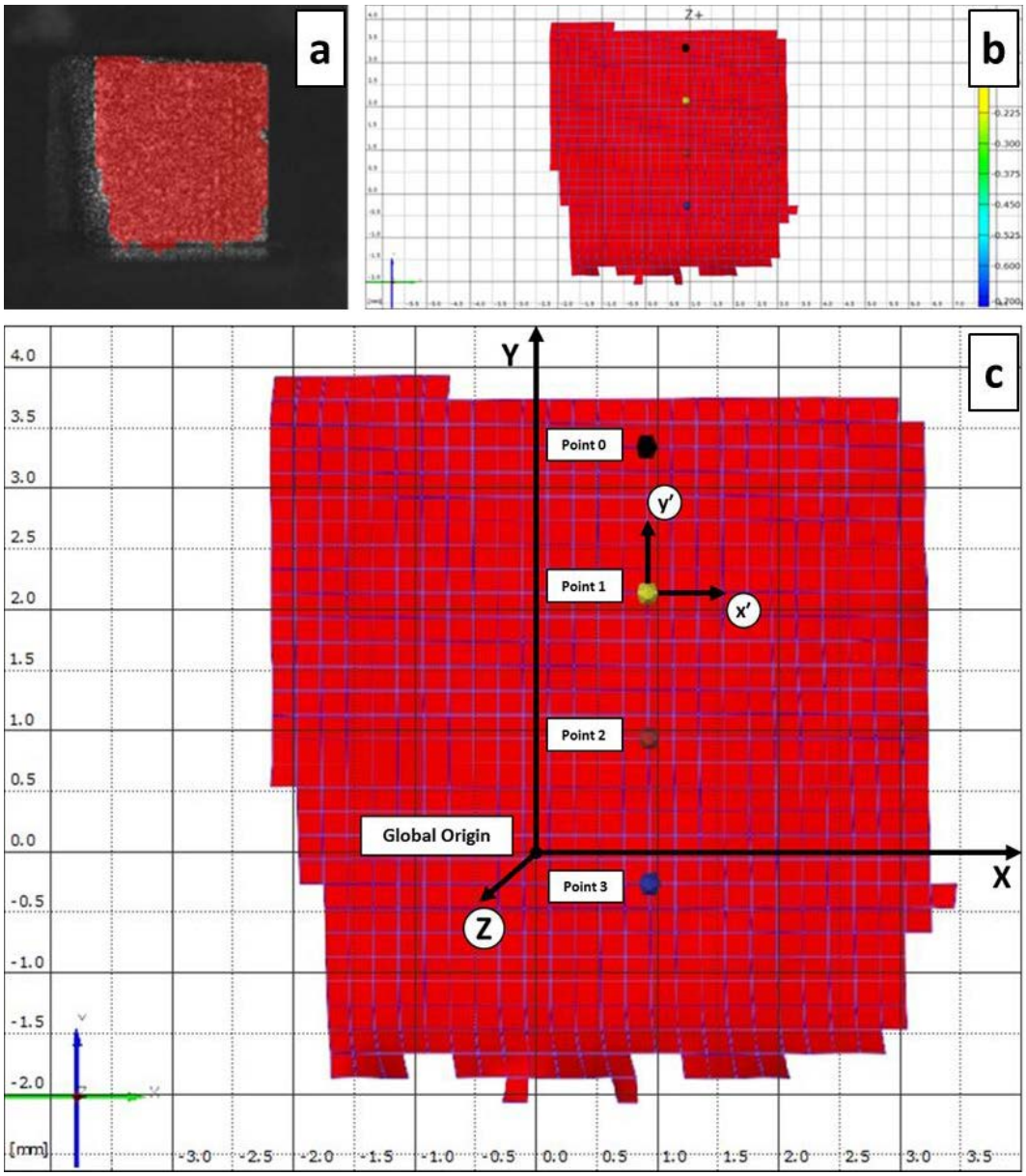

Figure 2 - 7: ARAMIS system: (a) AM Ni-Mn-Ga sample with overlaid grid; (b) Sample grid overlay (subsets are marked by red squares divided by blue grid); (c) ARAMIS global coordinate system (XYZ). Local coordinate system (x′y′z′) is also shown.

Data was recorded by following the displacement of the four points marked vertically on the sample's surface, shown in Figure 2-7c. Unlike the Arion 1D, which measures strain in real time, strain must be measured in post processing for the ARAMIS system. This is due to both the large quantity of data that the system tracks, as well as to the system data

processing. As mentioned before, a global coordinate system (XYZ) is assigned to the grid, and each subset can be imagined to have its own local coordinate system (x′y′z′). An example of a subset is illustrated in Figure 2-8. Movement is measured in pixels, so the accuracy of the measurement is dependent on the resolution of the cameras being used. Images are converted to binary where every pixel is either considered black (gray level 0) or white (grey level 100)[25].

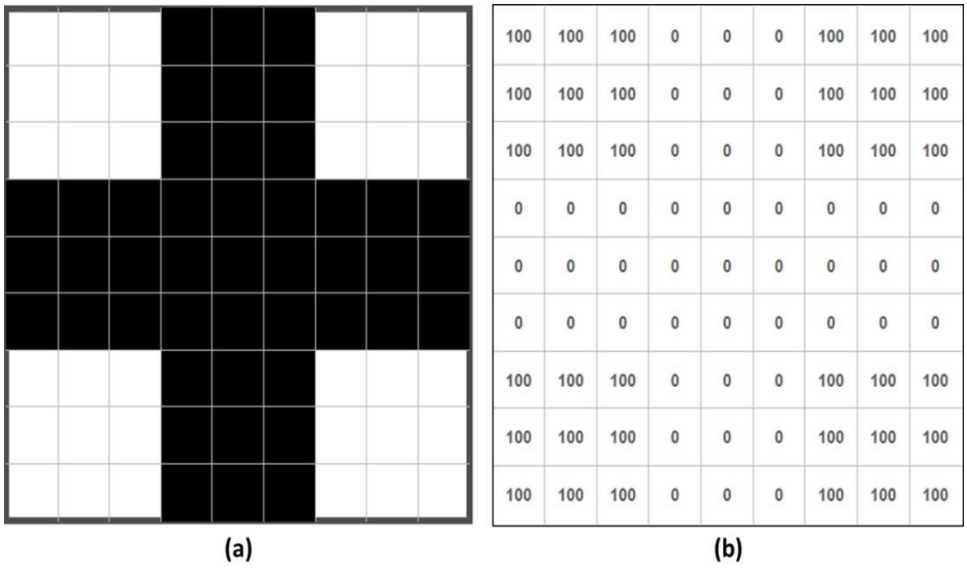

Figure 2 - 8: ARAMIS subset image: (a) Image on screen; (b) Image in memory[25].

If the image were to move one pixel up and one pixel to the right, the image after the motion would be like that of Figure 2-9.

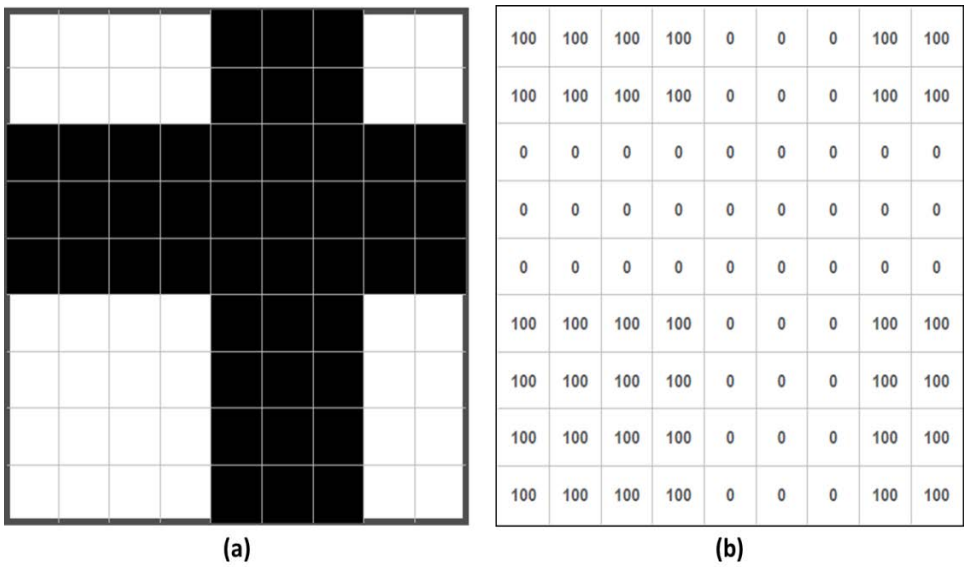

Figure 2 - 9: ARAMIS subset image motion: (a) Image after motion on screen; (b) Image after motion in memory[25].

Individual pixels are not unique making them hard to track. For this reason, pixels are grouped into reference frames which are more recognizable and easier for the ARAMIS system to follow. Reference frames are matrices of natural numbers created within each subset like shown in Figure 2-10.

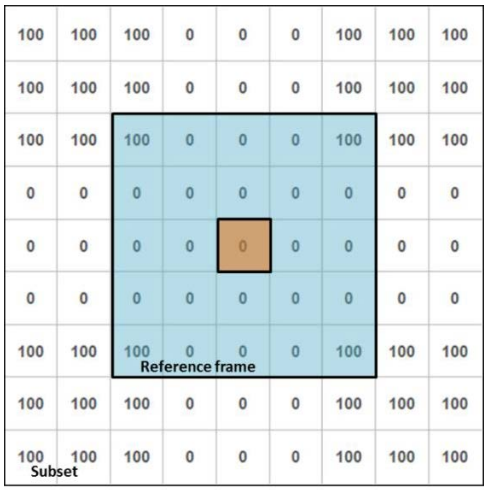

Figure 2 - 10: Reference frame within a subset[25].

A correlation function is then written to track this movement relative to the original position.

$$C(x,y,u,v) = \sum_{i,j=-\frac{(n-1)}{2}}^{\frac{(n-1)}{2}} \left(I(x+i,y+j) - I'(x+u+i,y+v+j)\right)^2 \qquad (2.1)$$

In this equation, *(x,y)* are the pixel coordinates of the center of the reference frame relative to the local coordinate system, (*u,v*) is the displacement (disparity), *n* is the reference frame size (5 in this case), *I* is the image before motion, and *I′* is the image after motion[22]. The ARAMIS system checks multiple values of *u* and *v* local to each reference frame, and considers the values corresponding to the lowest yielding value, *C*, as the actual movement of the frame. In other words, the *I* value that is closest to the *I′* value. To illustrate the use of this equation, using the current example shown in Figure 2-10, the reference frame centered at the (*x,y*) = (5,5) is moved (*u,v*) = (1,1).

Figure 2 - 11: Accurate tracking of reference frame[25].

Solving for C(5,5,1,1) the answer would be 0.

$$C(5,5,1,1) = \sum_{i,j=-2}^{2}\left(I(5+i,5+j) - I'(5+1+i,5+1+j)\right)^2 \tag{2.2}$$

$$C(5,5,1,1) = \left(\begin{bmatrix} 100 & 0 & 0 & 0 & 100 \\ 0 & 0 & 0 & 0 & 0 \\ 0 & 0 & 0 & 0 & 0 \\ 0 & 0 & 0 & 0 & 0 \\ 100 & 0 & 0 & 0 & 100 \end{bmatrix} - \begin{bmatrix} 100 & 0 & 0 & 0 & 100 \\ 0 & 0 & 0 & 0 & 0 \\ 0 & 0 & 0 & 0 & 0 \\ 0 & 0 & 0 & 0 & 0 \\ 100 & 0 & 0 & 0 & 100 \end{bmatrix}\right)^2 = 0 \tag{2.3}$$

The value of $C(5,5,1,1)$ is zero because the I is the same as I'. This means that (u,v) = (1,1) is the actual movement of the material relative to the local coordinate system. Comparatively, another potential value of (u,v) = (-2,-2) would be discarded by the ARAMIS system when compared to (u,v) = (1,1) since it yields a greater value, C. This can be seen in Figure 2-12 and Equation 2.6.

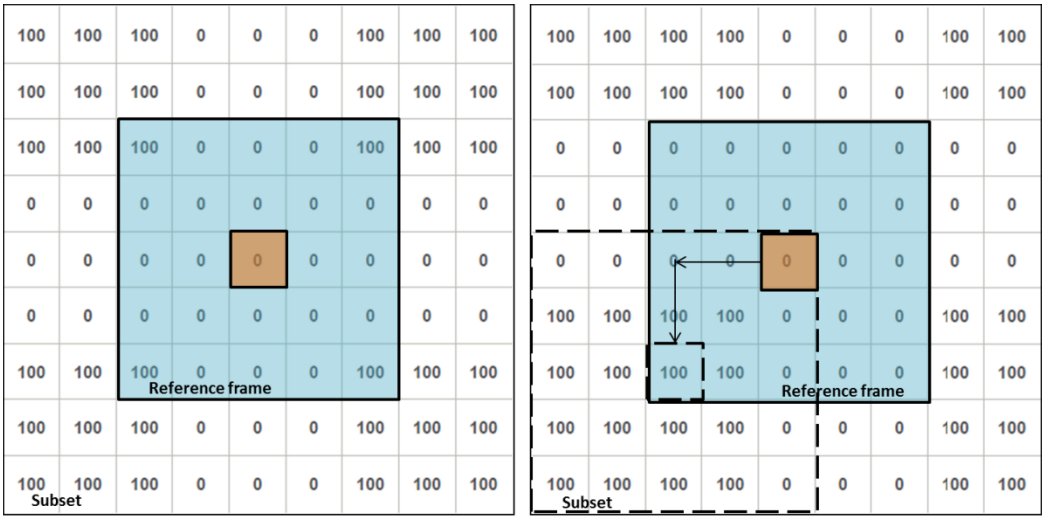

Figure 2 - 12: Inaccurate tracking of reference frame[25].

$$C(5,5,-2,-2) = \sum_{i,j=-2}^{2}\left(I(5+i,5+j) - I'(5-2+i,5-2+j)\right)^2 \quad (2.4)$$

$$C(5,5,1,1) = \left(\begin{bmatrix} 100 & 0 & 0 & 0 & 100 \\ 0 & 0 & 0 & 0 & 0 \\ 0 & 0 & 0 & 0 & 0 \\ 0 & 0 & 0 & 0 & 0 \\ 100 & 0 & 0 & 0 & 100 \end{bmatrix} - \begin{bmatrix} 0 & 0 & 0 & 0 & 0 \\ 100 & 100 & 100 & 100 & 0 \\ 100 & 100 & 100 & 100 & 0 \\ 100 & 100 & 100 & 100 & 0 \\ 100 & 100 & 100 & 100 & 0 \end{bmatrix}\right)^2 = 18{,}000 \quad (2.5)$$

$$C(5,5,1,1) \ll C(5,5,-2,-2), so\ (u,v) \neq (-2,-2) \quad (2.6)$$

During data acquisition, the pattern may become lighter or darker when compressed or expanded, or the movement is so small it cannot be measured in pixels. The ARAMIS system then uses interpolation techniques and optimization algorithms to continue to find the best value of *C* which correlates with the correct movement measurement[25].

2.3.2 Polar Decomposition Theorem

For both the Arion 1D and the ARAMIS system, the polar decomposition theorem is utilized to measure displacement and strain. As mentioned before, the polar decomposition theorem uses the principal stretches between the fiduciaries, or in the case of the ARAMIS system, between the origin of the global coordinate system and each subset. The principal stretches are treated as body particle motion which can be expressed as a rigid rotation followed by a pure deformation and vice versa[28]. The process to derive this stretch is the same.

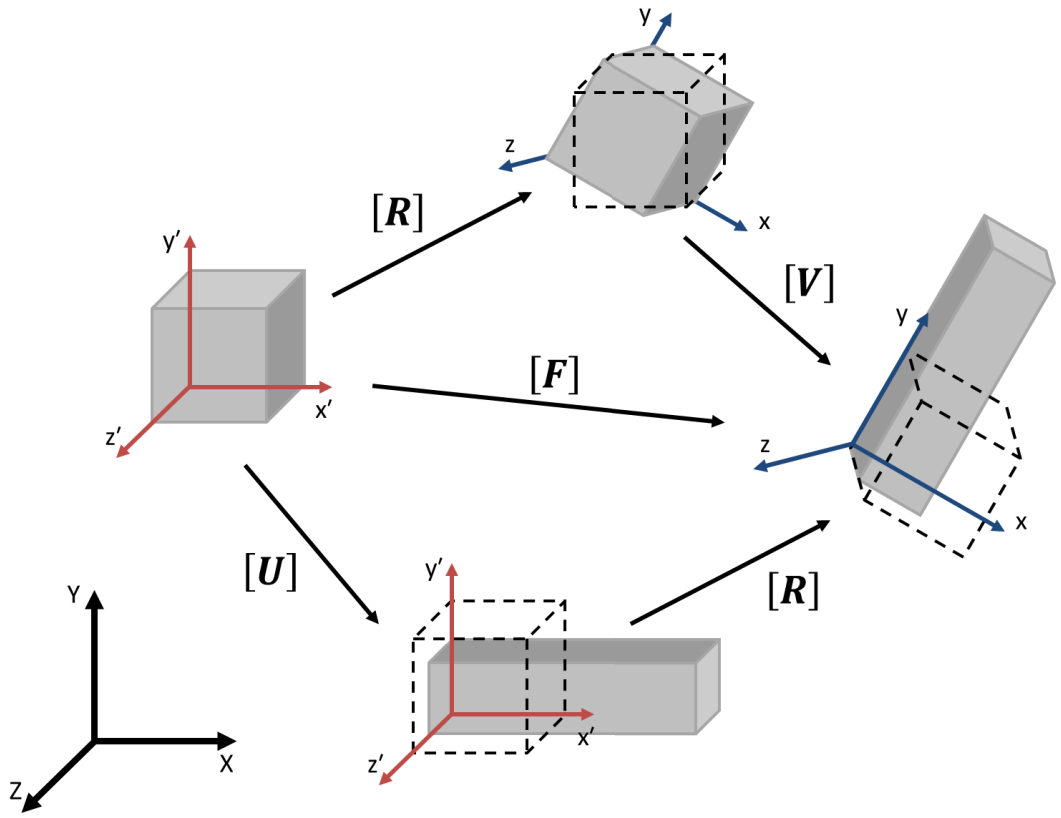

Figure 2 - 13: Polar decomposition theorem.

Polar Decomposition Theorem: $\boldsymbol{F = RU = VR}$ (2.7)

Where: $\boldsymbol{R}$ is the *proper orthogonal rotation matrix*
$\boldsymbol{U}$ is the *right* stretch tensor
$\boldsymbol{V}$ is the *left* stretch tensor

$$Deformation\ Gradient: \boldsymbol{F} = \frac{\partial(x,y,z)}{\partial(X,Y,Z)} = \begin{bmatrix} \frac{\partial x}{\partial X} & \frac{\partial x}{\partial Y} & \frac{\partial x}{\partial Z} \\ \frac{\partial y}{\partial X} & \frac{\partial y}{\partial Y} & \frac{\partial y}{\partial Z} \\ \frac{\partial z}{\partial X} & \frac{\partial z}{\partial Y} & \frac{\partial z}{\partial Z} \end{bmatrix} \quad (2.8)$$

Where: $\boldsymbol{x}$ is the spatial global frame
$\boldsymbol{X}$ is the material global frame

The displacement of the four points marked in Figure 2-7 was the data gathered by the ARAMIS system. The displacement gradient is the same as the deformation gradient minus the identity matrix.

$$Displacement\ Gradient: \boldsymbol{G} = \boldsymbol{F} - \boldsymbol{I} = \begin{bmatrix} \frac{\partial x}{\partial X} - 1 & \frac{\partial x}{\partial Y} & \frac{\partial x}{\partial Z} \\ \frac{\partial y}{\partial X} & \frac{\partial y}{\partial Y} - 1 & \frac{\partial y}{\partial Z} \\ \frac{\partial z}{\partial X} & \frac{\partial z}{\partial Y} & \frac{\partial z}{\partial Z} - 1 \end{bmatrix} \tag{2.9}$$

The rotation of the coordinate system, as indicated in Figure 2-14, must also be taken into account.

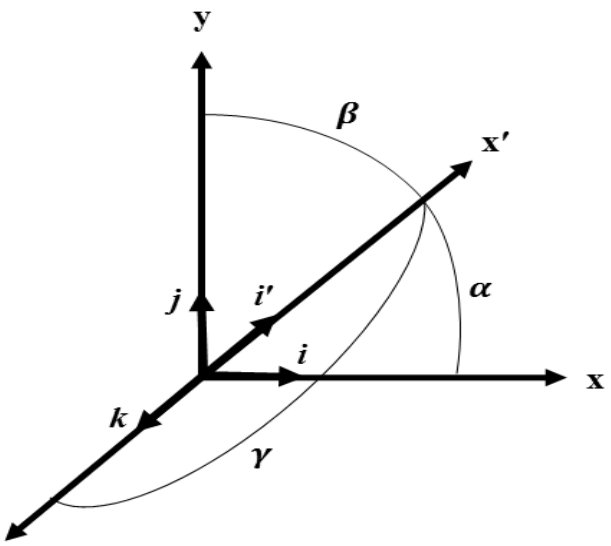

Figure 2 - 14: Rotation of coordinate system xyz to x′y′z′.

$$\cos\alpha = (\boldsymbol{i}' \cdot \boldsymbol{i})\ ;\ \cos\beta = (\boldsymbol{i}' \cdot \boldsymbol{j})\ \ ;\ \ \cos\gamma = (\boldsymbol{i}' \cdot \boldsymbol{k}) \tag{2.10}$$

$$\boldsymbol{i}' = (\boldsymbol{i}' \cdot \boldsymbol{i})\boldsymbol{i} + (\boldsymbol{i}' \cdot \boldsymbol{j})\boldsymbol{j} + (\boldsymbol{i}' \cdot \boldsymbol{k})\boldsymbol{k}$$

$$\boldsymbol{j}' = (\boldsymbol{i}' \cdot \boldsymbol{i})\boldsymbol{i} + (\boldsymbol{j}' \cdot \boldsymbol{j})\boldsymbol{j} + (\boldsymbol{j}' \cdot \boldsymbol{k})\boldsymbol{k}$$

$$\boldsymbol{k}' = (\boldsymbol{k}' \cdot \boldsymbol{i})\boldsymbol{i} + (\boldsymbol{k}' \cdot \boldsymbol{j})\boldsymbol{j} + (\boldsymbol{k}' \cdot \boldsymbol{k})\boldsymbol{k}$$

The above expressions indicate that the cosines of the direction angle are the most significant for the analysis of the rotation matrix.

$$\left.\begin{array}{c}\textbf{If: } p = x\ ;\ p' = x' \\ q = x, y, or\ z \\ \textbf{If: } p = y\ ;\ p' = y' \\ q = x, y, or\ z \\ \textbf{If: } p = z\ ;\ p' = z' \\ q = x, y, or\ z\end{array}\right\} \boldsymbol{l_{p'q}} = \cos\left(\tan^{-1}\left(\frac{p'}{q}\right)\right) \tag{2.11}$$

Proper Orthogonal Rotation Matrix: $\boldsymbol{R} = \begin{bmatrix} l_{x'x} & l_{x'y} & l_{x'z} \\ l_{y'x} & l_{y'y} & l_{y'z} \\ l_{z'x} & l_{z'y} & l_{z'z} \end{bmatrix}$ (2.12)

Where: $\boldsymbol{R}^{-1} = \boldsymbol{R}^T\ ;\ \ \det(\boldsymbol{R}) = 1$

$Stretch\ Tensors$: $\left.\begin{array}{l}\boldsymbol{U} = \lambda_i \phi_i \phi_i^T \\ \boldsymbol{V} = \lambda_i \psi_i \psi_i^T\end{array}\right\}$ Symmetric Positive-Definite Matrices

Where: λ_i are the eigenvalue principle stretches, Figure 2-15.
ϕ_i and ψ_i are orthonormalized eigenvectors representing principle directions.

$$\psi_i \psi_i^T = \phi_i \phi_i^T = \{\boldsymbol{s}\} \tag{2.13}$$

$$\begin{aligned}[\boldsymbol{U}]\{\boldsymbol{s}\} &= \boldsymbol{\lambda}\{\boldsymbol{s}\} \\ [\boldsymbol{U} - \lambda \boldsymbol{I}]\{\boldsymbol{s}\} &= \boldsymbol{0}\end{aligned} \tag{2.14}$$

Where: $\{\boldsymbol{s}\} \neq 0$ to avoid trivial solution.

$$\boldsymbol{U} = \lambda \boldsymbol{I} = \begin{bmatrix} \lambda_x & 0 & 0 \\ 0 & \lambda_y & 0 \\ 0 & 0 & \lambda_z \end{bmatrix} \tag{2.15}$$

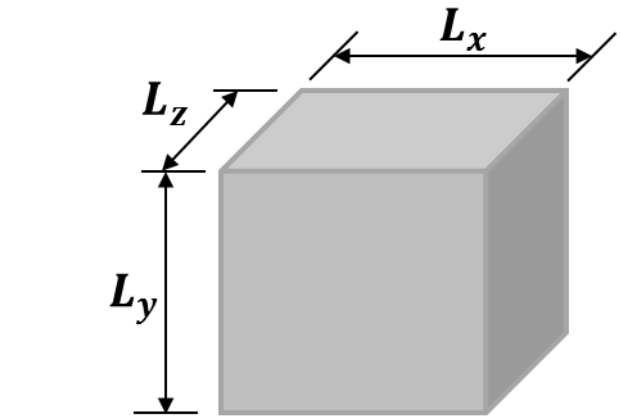

Figure 2 - 15: Eigenvalue principle stretches.

Calculation of the Lagrangian stretch tensor from equation 2.7, is as follows.

$$F = RU$$
$$F^T \cdot F = F^T \cdot RU$$
$$F^T \cdot F = (RU)^T \cdot RU = U^T R^T RU$$

Because the rotation matrix is orthogonal, $R^T R = I$. Thus,

$$\boldsymbol{U^2 = F^T \cdot F} \tag{2.16}$$

Similarly: $\boldsymbol{V^2 = F \cdot F^T}$

$\mathbf{C}_R = \mathbf{U}^2$: Lagrangian (or material) stretch tensor
$\mathbf{C}_L = \mathbf{V}^2$: Eulerian (or spatial) stretch tensor

The Lagrangian stretch tensor is then used to calculate either Green-Lagrange or Henky strain.

$$\varepsilon^G = \frac{1}{2}(C_R - I) \quad \left(Green - Lagrange; used\ by\ ARAMIS^{29}\right) \tag{2.17}$$

$$\varepsilon^H = \frac{1}{2}\log(C_R) \quad (Henky; used\ by\ UVID^{26}) \tag{2.18}$$

CHAPTER 3: NUMERICAL METHODS

3.1 Overview of numerical modeling of porous materials

The benefits porosity lends to FSMA such as increased magnetic field induced strain (MFIS), are very exciting, yet the drawback is also significant. For example, it seems to make the material even more brittle than in the case of bulk polycrystalline Ni-Mn-Ga . In the case of AM parts, stress risers are created at the sharp corners of the voids which significantly decrease the parts' mechanical integrity. Therefore, compared to a bulk samples, AM samples have completely different mechanical properties. This is presumably also true for the magnetic properties of the material, but experimentation to validate this was beyond the scope of this research. Voids contribute to unpredictability in stress and strain distribution in the parts. Current means of modeling SMAs are ineffective because of this characteristic.

In this work, a SEM micrograph of the polished surface of an AM part was converted into a CAD surface body geometry then tested using finite element analysis software. This analysis can then be used to visualize and measure the effect porosity has on the stress, strain, and magnetization of an additively manufacture FSMA part. Like the approach taken by the literature written for metallic foams (Čapek *et al*.[30]; Hernández-Nava *et al*.[31]; Brothers and Dunand[32]), the AM parts are treated as independent, bulk composite material (two interpenetrating networks of void and metal) and given their own mechanical properties. Based on the load and the displacement of the moving

crosshead of the Instron testing system, stress-strain relationships are calculated and used to determine the mechanical properties of this composite material, such us the Young's modulus and the yield strength. By comparing the experimental stress-strain behavior of AM parts to the theoretical stress-strain behavior of the Finite Element Analysis (FEA) micrograph-based model, the mesh of the model can potentially be validated. This should be used in conjunction with conventional convergence methods for validating and FEA model.

3.2 Converting a scanning electron micrograph into geometry for finite element analysis

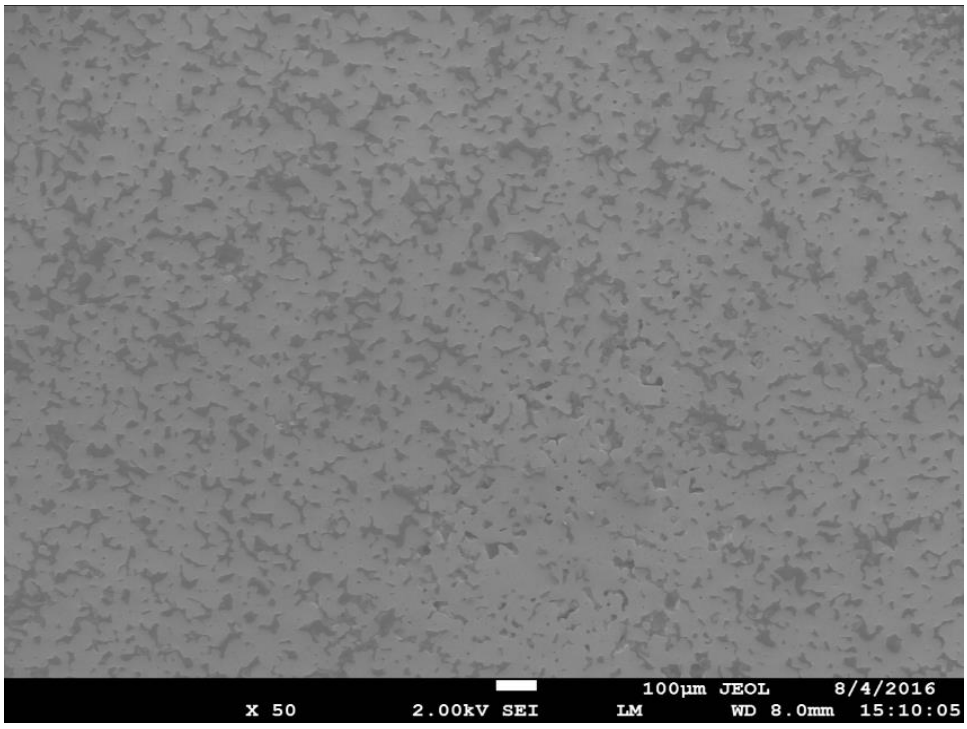

Figure 3 - 1: Secondary electron micrograph of additively manufactured Ni-Mn-Ga. The dark regions of the micrograph are the voids in the material.

Figure 3-1 shows the scanning electron micrograph used as the initial data in the modeling process. It is important to know the total dimensions of the original micrograph to be able to later check the final surface body generated for the FEA model. The micrograph in Figure 3-1 was inserted into AutoCAD as a *Raster Image Reference*. The dimensions of the imported image are out of scale and the AutoCAD units in this step are irrelevant. To find the actual dimensions of the image, the scale bar of the JEOL micrograph (100 μm) was measured, then used to scale the rest of the image . This is shown in Figure 3.2 and Equations 3.1 and 3.2.

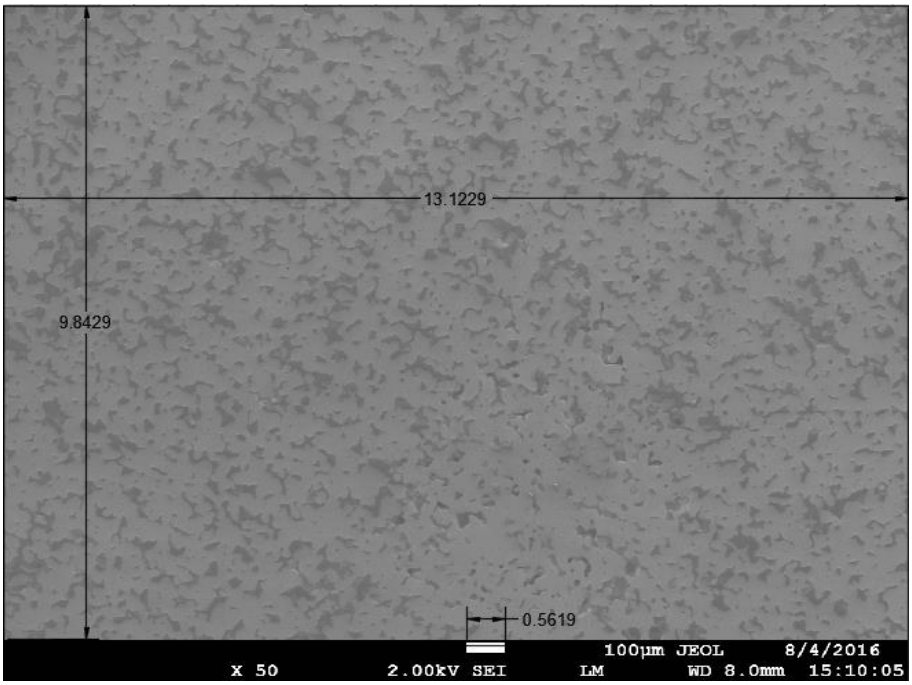

Figure 3 - 2: Micrograph dimensions measured in AutoCAD. The 100 μm scale bar measures to be 0.5619 AutoCAD units.

Height: $\frac{0.5619\ AutoCAD\ units}{100\mu m} = \frac{9.8429\ AutoCAD\ units}{h} \rightarrow \boldsymbol{h = 1751.7174\ \mu m}$ (3.1)

Width: $\frac{0.5619\ AutoCAD\ units}{100\mu m} = \frac{13.1229\ AutoCAD\ units}{w} \rightarrow \boldsymbol{w = 2335.4511\ \mu m}$ (3.2)

The ultimate goal is to trace the perimeters of these voids in a format that can be read by AutoCAD as a series of organized, properly spaces polylines. To do this, it is beneficial to further increase the contrast between the material and the voids. This was done in Adobe Photoshop using the *posterize* feature, Figure 3-3. This feature can be used to reduce the number of tones in the image to two: black and white, Figure 3-3 (b).

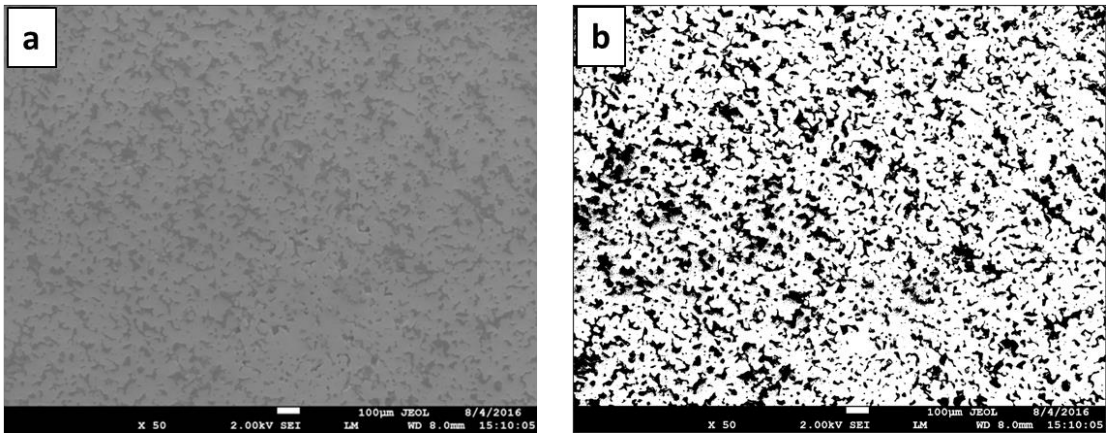

Figure 3 - 3: (a) Original micrograph; (b) Posterized image.

The binary, black and white image was saved as a Tag Image Format (TIF) file to preserve as much detail as possible. Then *Convertio*[33], a free online file converting tool, was utilized to convert the TIF file into the Drawing Exchange Format (DXF) file which could be opened in AutoCAD, Figure 3-4.

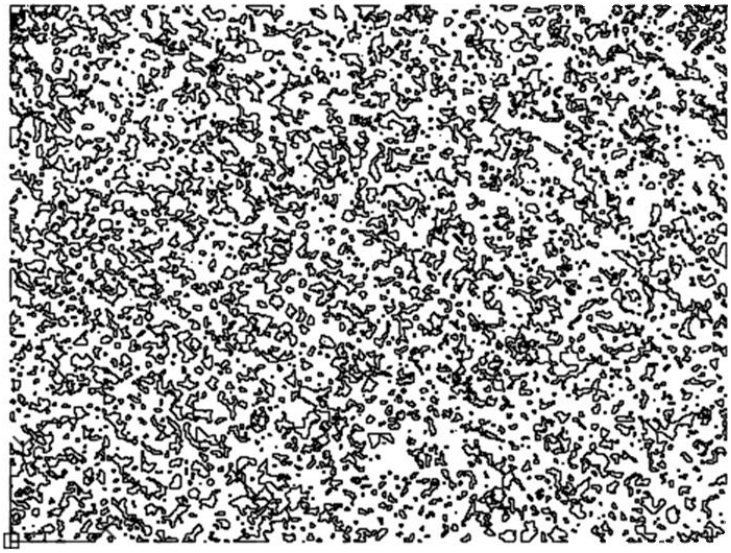

Figure 3 - 4: DXF file imported into AutoCAD.

The CAD software is needed for converting the polylines used to trace the void into surface bodies that can be read in ANSYS Workbench. The current dimensions of the DXF file will be in pixels, so the image must first be rescaled to the measurements taken of the original micrograph, Equations 3.1 and 3.2. The image must then be sectioned into smaller sample sizes that can be meshed in ANSYS and run efficiently, Figures 3-5 and 3-6.

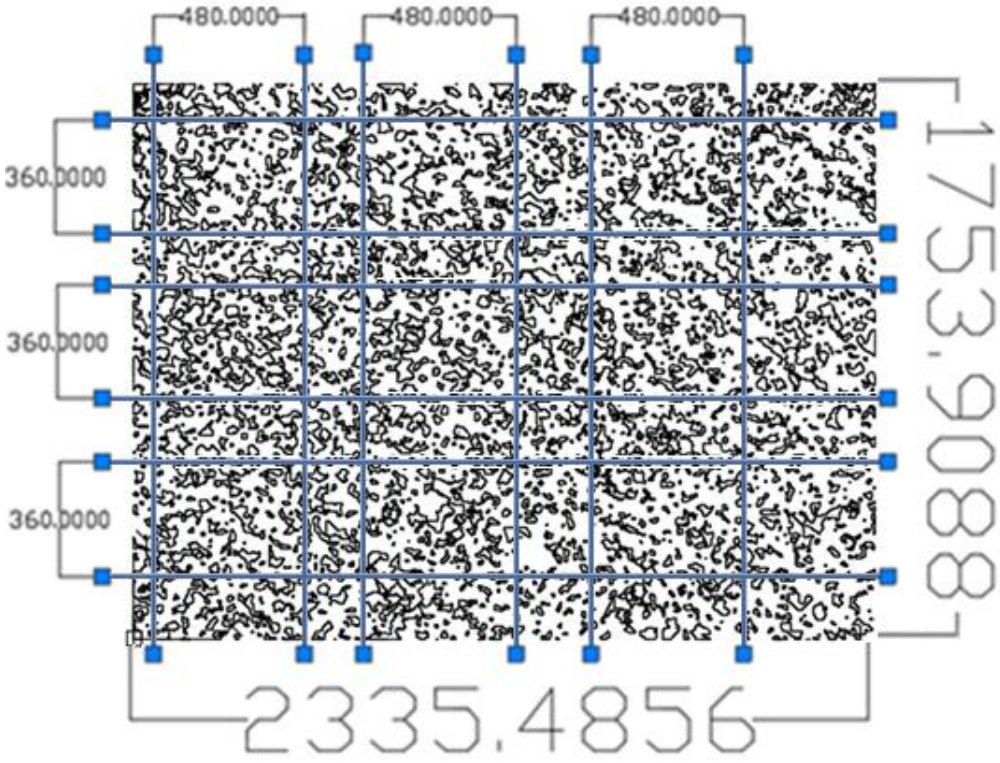

Figure 3 - 5: DXF file scaled back to original dimensions. Lines are drawn to divide it into smaller samples.

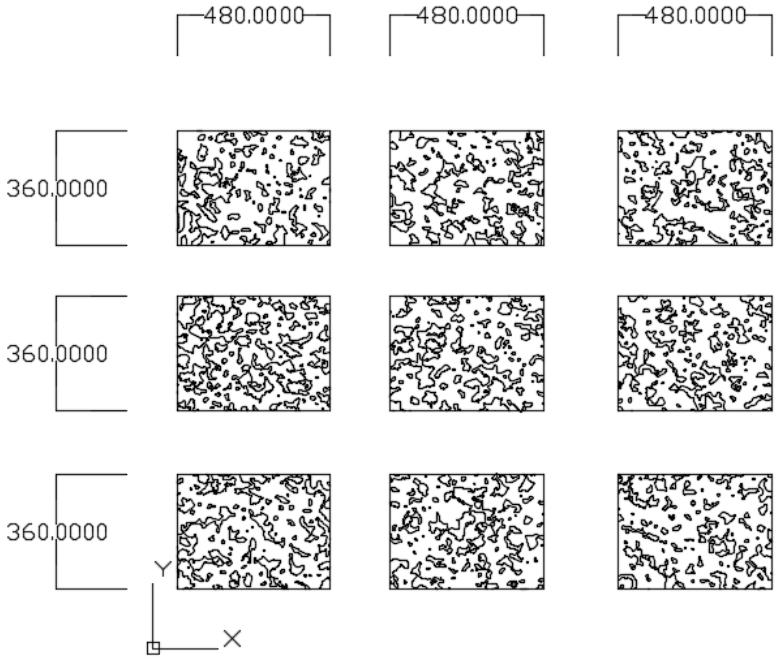

Figure 3 - 6: Image divided into smaller, equivalent sections.

Further, the polylines used to trace the voids are converted into surface bodies, as shown in Figure 3-7.

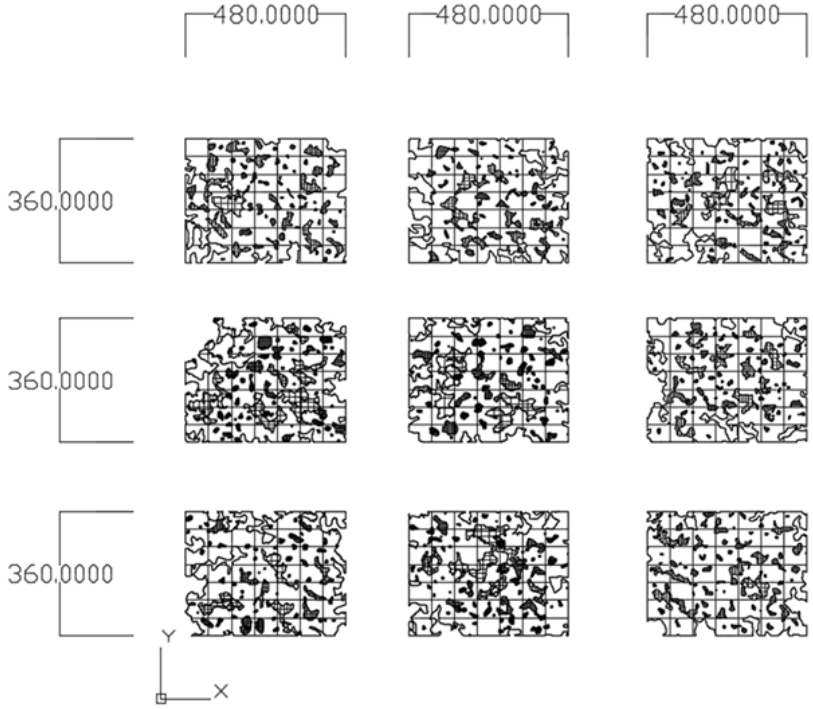

Figure 3 - 7: Polylines converted to surface bodies.

These surface bodies must be exported individually as Standard ACIS Text (SAT) files which can be imported into ANSYS Workbench as external geometry files. The voids will be imported as surfaces as well, but these can be cut from the body using the extrude feature in the Geometry window in ANSYS Workbench.

3.3 Engineering Data for ANSYS Workbench

Based on the experimental results for the mechanical properties of the bulk Ni-Mn-Ga, documented in Chapter 4, the following material inputs were used for both bulk and AM models, shown in Figure 3-8.

Properties of Outline Row 4: Ni-Mn-Ga (Bulk)

	A	B	C	D	E
1	Property	Value	Unit		
2	Density	7.388	g cm^-3		
3	Isotropic Elasticity				
4	Derive from	Young's Modulus and Poisson's...			
5	Young's Modulus	16585	MPa		
6	Poisson's Ratio	0.3			
7	Bulk Modulus	1.3821E+10	Pa		
8	Shear Modulus	6.3788E+09	Pa		
9	Superelasticity				
10	Sigma SAS	142	MPa		
11	Sigma FAS	379	MPa		
12	Sigma SSA	379	MPa		
13	Sigma FSA	142	MPa		
14	Epsilon	0.00366	m m^-1		
15	Alpha	0			

Figure 3 - 8: Engineering data for ANSYS Workbench.

3.4 Model Geometry for Compressive Testing

To simplify the modeling in ANSYS Workbench just one section of the initial surface was selected, see Figures 3-6 and 3-7. The moving crosshead of the Instron was added to the model with the shaft being the same width (480 μm) as the sample (selected section) itself. This serves not only as the driving displacement to simulate the compressor in the experiment, but it also measures the magnitude of the uniform equivalent stress of the AM part, considered as a bulk body. In the case of 100% dense material this feature is unnecessary, but it was used in order to note one inaccuracy of this technique, as can be seen in Figure 3-9. Because the compressor is made of steel, not Ni-Mn-Ga, it does not deform laterally as much as the sample. This means it will show a stress value slightly higher than that in the sample since its area will be smaller by the end of the test. This difference in lateral expansion is also the reason the compressor has the wide head at the sample interface. Because Ni-Mn-Ga is so brittle, any lateral expansion resulting in significant disparities between the stress value in the compressor and the sample will result in fracturing of the sample. Therefore, by using a wide head compressor, this difference (1.77%, as seen in Figure 3-9) will be neglected. It is worth noting that the compressor was made twice as tall as the width of the sample. This ensures the stress near the middle of the compressor is equal to the average stress being applied to the sample, suggested by Saint Venant's Principle for accuracy.

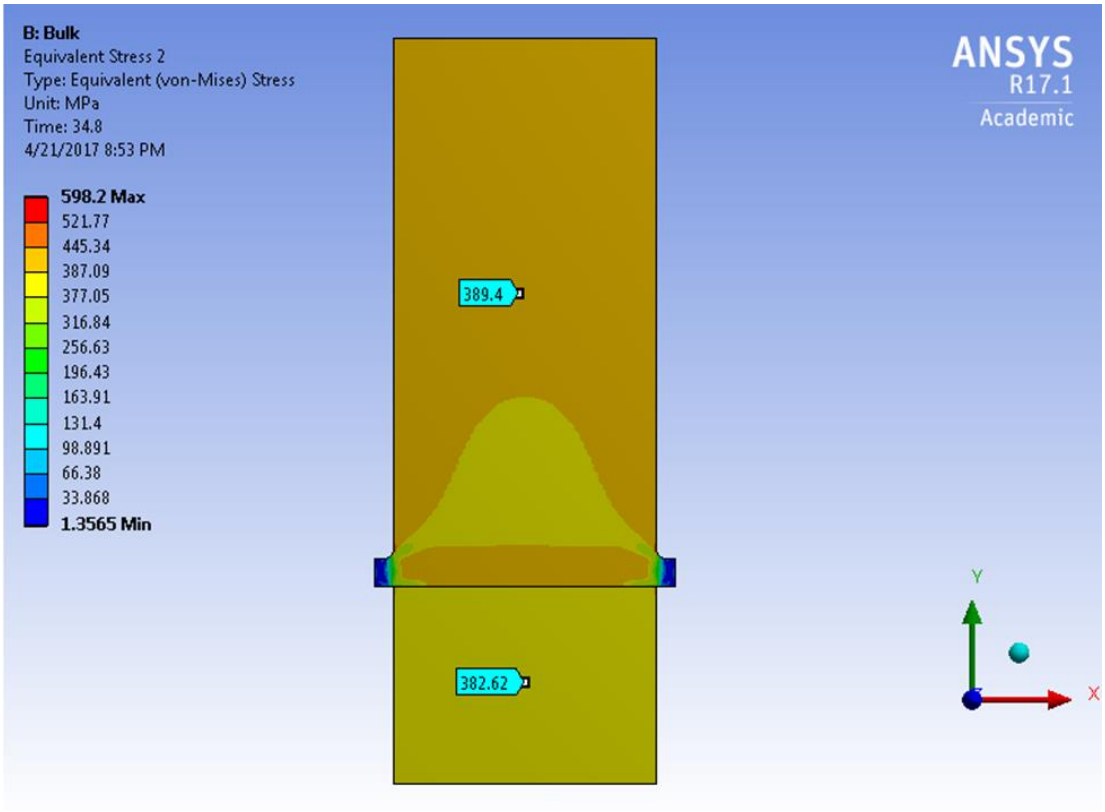

Figure 3 - 9: Stress in the bulk Ni-Mn-Ga sample at failure compared to the stress in the compressor (percent error = 1.77%).

The bulk sample was modeled first to ensure the accuracy of the material inputs. The bulk sample has the same dimensions as the AM models (480 μm x 360 μm). The boundary conditions for the bulk sample are shown in Figure 3-10. The boundary conditions for the AM sample are the same as for bulk sample, and the compression model for this sample is shown in Figure 3-11.

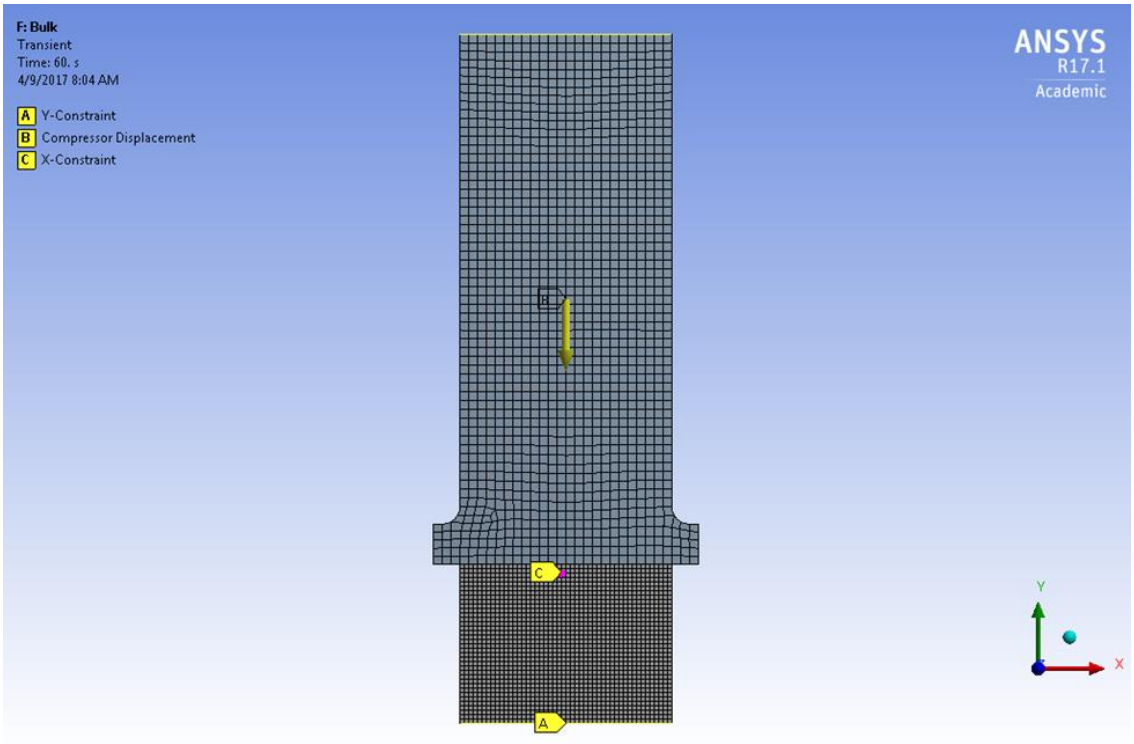

Figure 3 - 10: Boundary conditions of bulk model: (a) Zero y-displacement; (b) Negative y-displacement of 20 µm over 60 seconds of uniform loading; (c) Zero x-displacement.

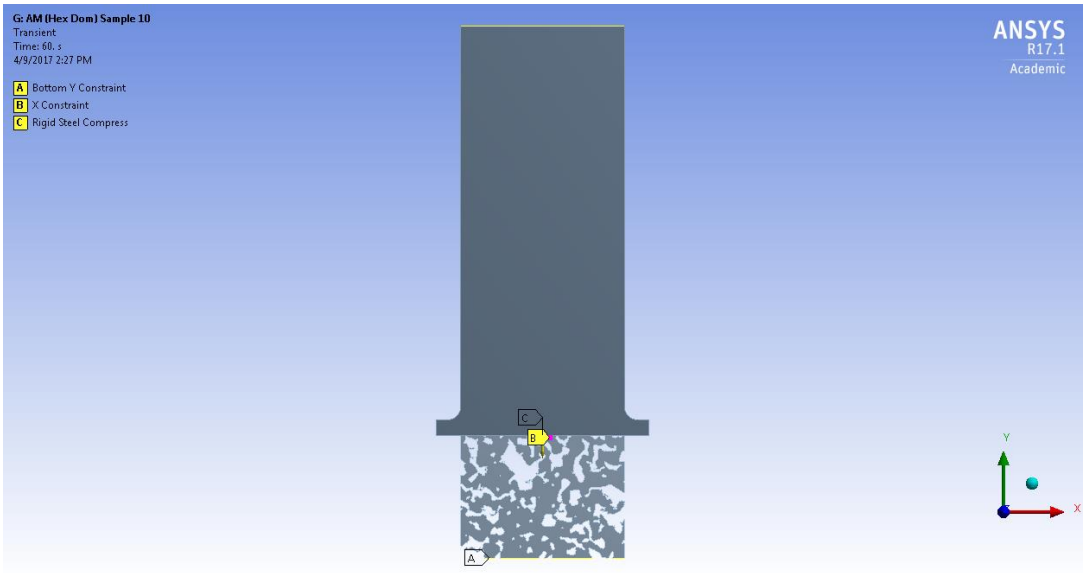

Figure 3 - 11: Boundary conditions for AM model are same as those for bulk model.

A “no separation” connection was used to connect the sample to the compressor. Next, a single node was constrained in the x-direction on the sample (C) to give the model stability and prevent rigid body motion in the x-direction. Then a zero y-displacement (a) was assigned to the bottom of the sample so that it could still deform laterally as it was compressed. Finally the compressor was displaced uniformly over 60 seconds to a total displacement of 20 μm.

For the bulk material, the numerical modeling results are compared to the experimental data, as shown in Figure 3-12. A good match was obtained between the experimental and numerical data.

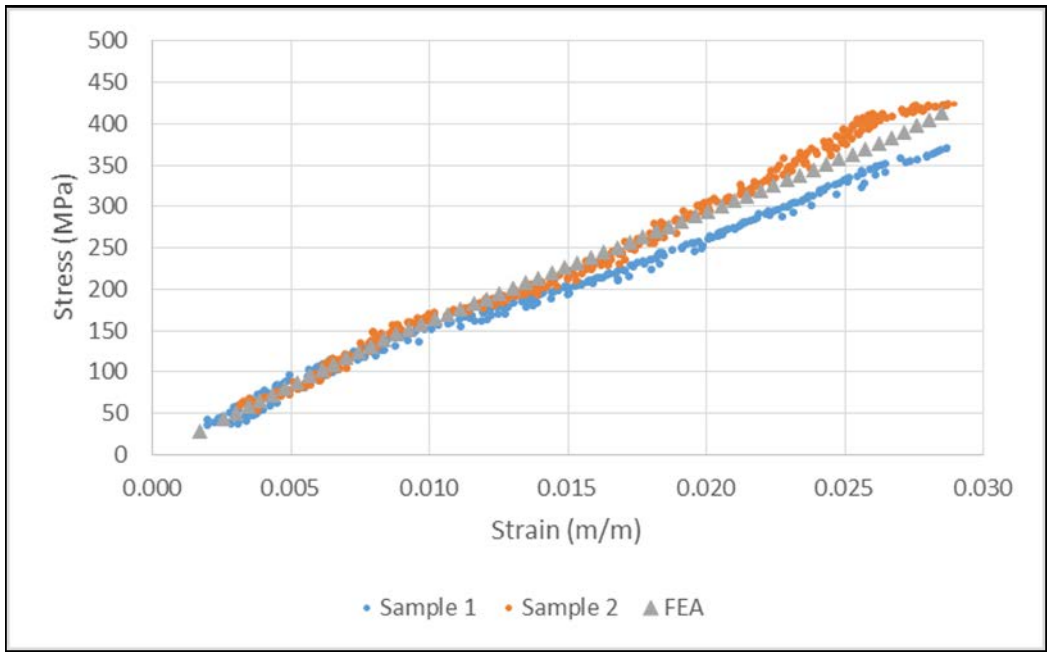

Figure 3 - 12: FEA results compared with experimental data of bulk Ni-Mn-Ga. Sample 1 and sample 2 data have been obtained from compression testing measurements, as reported in Chapter 4.

3.5 Meshing in ANSYS Workbench

Because the mesh of the bulk sample is made of near perfect squares, and since its results match the experimental data, a convergence test is not needed and the model is known to be accurate. For the AM model, the mesh had to be manipulated to ensure it accurately capture the events within the model. Ideally, to know a mesh is accurate, the mesh size should continuously be refined until the results show the same value. This method is a known as a convergence test. However, due to licenses limitations, the finest mesh was constricted to 256,000 elements, and convergence could not be proved[34]. However, to validate the model, element quality checks were performed using ANSYS's orthogonality and skewness quality features, and the model data was compared with experimental data.

3.5.1 Quality Meshing

The general idea behind finite element analysis is taking a large complex shape that cannot be represented theoretically and dividing it into numerous cells with shapes that can be represented in mathematical form. These divisions are known as elements which make up the model's mesh. A quality mesh is one major key to the accuracy of any FEA model, so it is important to know how the meshing works in an FEA package. The basic concept of a mesh is adjacent cells, or elements, share faces and edges with one another, as well as nodes, in the places where more than one edge comes together. Equations used in the simulation of an FEA model are solved at cell/nodal locations. The temperature or stress state of each element is the average of the effects of the adjacent elements around it. For example, if a cantilever beam with a load at its end is being modeled only two

elements thick, the stress at any point along the cantilever would be zero. This is because the top surface at any distance from the load is stressed in tension, while the bottom surface at the same distance has the same magnitude of stress but in compression. Because these elements touch, they negate one another. In the cantilever example, more elements must be introduced to the thickness of the beam in order to capture the necessary details. In other words, the mesh needs to be refined. The finer the geometric detail at a particular location within a model, the finer the mesh at that location needs to be.

There's a variety of element shapes that can be used to build the mesh, some better than others. These shapes include triangles and squares for 2D geometries, and tetrahedrons, prisms, pyramids, and hexahedra for 3D geometries. As a general rule, the more faces and nodes an element shares, the more accurate that element is. As was mentioned previously, the result of each element is an average of the elements adjacent to it, so the more faces an element shares with the ones around it, the better it represents that location on the real part. The highest quality elements are made entirely up of equilateral triangles and perfect squares. It is easier to get a mesh of quality triangular/tetrahedral elements as the piece together easier, but square/hexagonal elements are more accurate being as they share more faces and nodes with the elements around them. This is an important detail to keep in mind when building a mesh. For the model used in this paper, square elements were used, and to check their quality, two of the major mesh metrics available in ANSYS Meshing*, orthogonal quality* and *skewness,* were observed[35].

3.5.2 Orthogonal Quality

In ANSYS, orthogonality is either measured "on cell" or "on face". *On cell* either refers to a vector from the centroid of the cell to the centroid of the face, or from the centroid of the cell to the centroid of the adjacent cell, Figure 3-13.

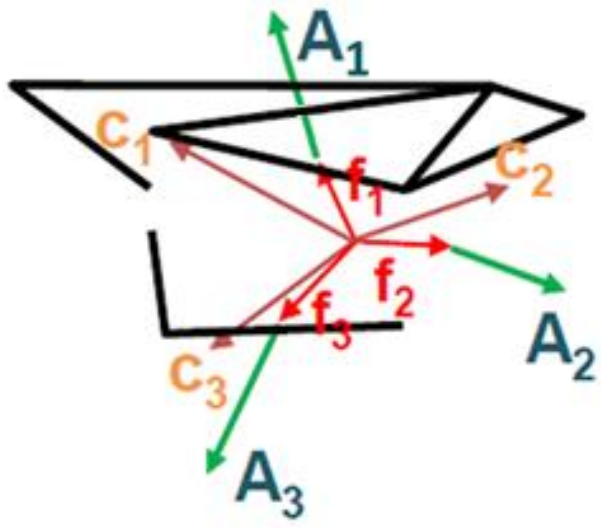

Figure 3 - 13: *On Cell*: A_i is the face-normal vector; f_i is a vector from the centroid of the cell to the centroid of that face; and c_i is a vector from the centroid of the cell to the centroid of the adjacent cell[35].

For *on cell*, the orthogonal quality is the minimum of: $\frac{A_i \cdot f_i}{|\vec{A}_i| \cdot |\vec{f}_i|}$ *or* $\frac{A_i \cdot c_i}{|\vec{A}_i| \cdot |\vec{c}_i|}$ (3.3)

On face refers to a vector from the centroid of the face to the centroid of the edge, Figure 3-14.

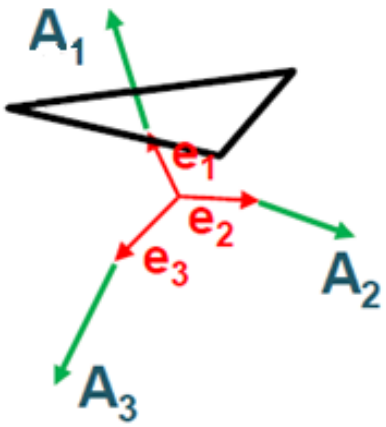

Figure 3 - 14: *On Face*: e_i is the vector from the centroid of the face to the centroid of the edge[35].

For *on face*, the orthogonal quality is the minimum of: $\frac{A_i \cdot e_i}{|\vec{A}_i| \cdot |\vec{e}_i|}$ (3.4)

Orthogonal quality is measured from 0 to 1, with 1 being the best. The mesh quality recommendations by Ozen Engineering, the ANSYS distributor to Northern California and the Silicon Valley are shown in Figure 3-15[35].

Unacceptable	Bad	Acceptable	Good	Very good	Excellent
0-0.001	0.001-0.14	0.15-0.20	0.20-0.69	0.70-0.95	0.95-1.00

Figure 3 - 15: Orthogonal quality mesh metrics spectrum[35].

The orthogonal quality of the mesh for the AM Ni-Mn-Ga model can be seen in Figure 3-16. Figure 3-17 shows the positions (dark areas) of the elements having the orthogonal quality below 0.8.

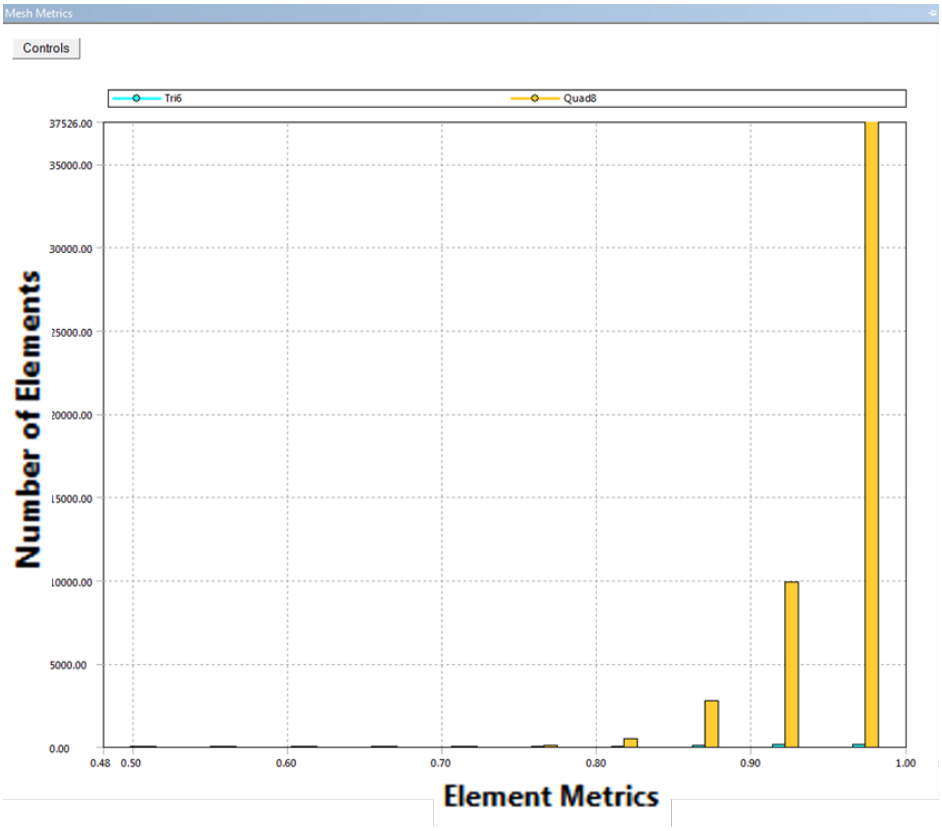

Figure 3 - 16: The orthogonal quality shows that the majority of the elements lie above 0.80 (very good quality). All elements shown are considered acceptable.

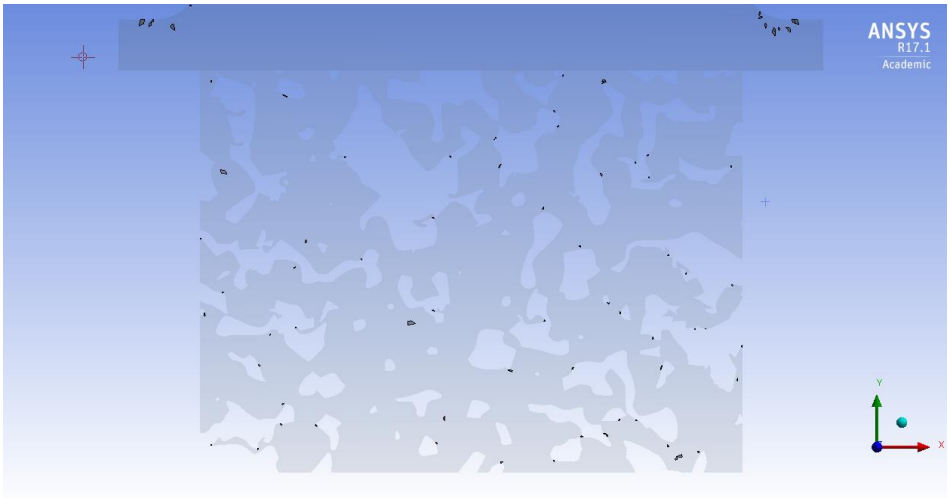

Figure 3 - 17: All elements with orthogonal quality below 0.80.

3.5.3 Skewness

There are two methods for determining the skewness of an element. The first is equilateral volume deviation, and the second is normalized angle deviation. Equilateral volume deviation applies to triangles and tetrahedrons only. It is the error percentage of the actual cell size to the optimal cell size. This principle is illustrated in Figure 3-18.

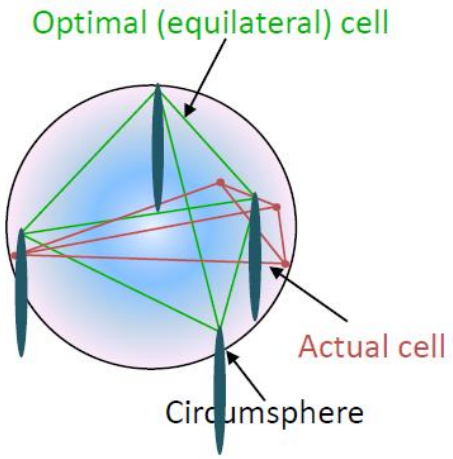

Figure 3 - 18: Skewness: equilateral volume[35].

$$Skewness = \frac{optimal\ cell\ size - cell\ size}{optimal\ cell\ size} \tag{3.5}$$

Normalized angle deviation is considered when quadrilaterals, pyramids, prisms, and hexahedra are present in the mesh. Skewness is found as follows.

$$Skewness = max\left[\frac{\theta_{max} - \theta_e}{180° - \theta_e}, \frac{\theta_e - \theta_{max}}{\theta_e}\right] \tag{3.6}$$

Where θ_e is the equiangular face/cell (60° for tetrahedrons and triangles, and 90° for quadrilaterals, pyramids, prisms, and hexahedra):

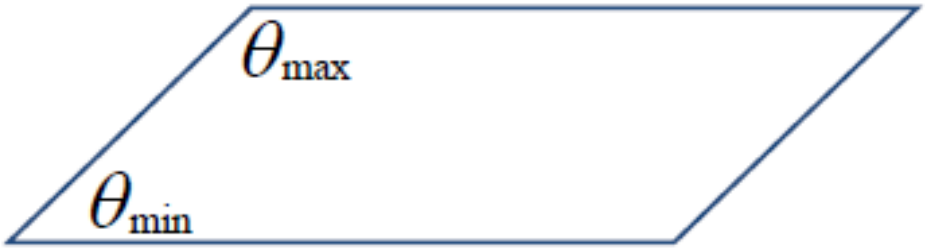

Figure 3 - 19: Skewness: normalized angle deviation[35].

Skewness is also measured from 0 to 1, but 1 is the worst. The mesh quality recommendations by Ozen Engineering is shown in Figure 3-20.

Excellent	Very good	Good	Acceptable	Bad	Unacceptable
0-0.25	0.25-0.50	0.50-0.80	0.80-0.94	0.95-0.97	0.98-1.00

Figure 3 - 20: Skewness mesh metrics spectrum[35].

The skewness of the mesh of the AM model can be seen in Figure 3-21. Figure 3-22 shows the positions (dark areas) of the elements having skewness above 0.5.

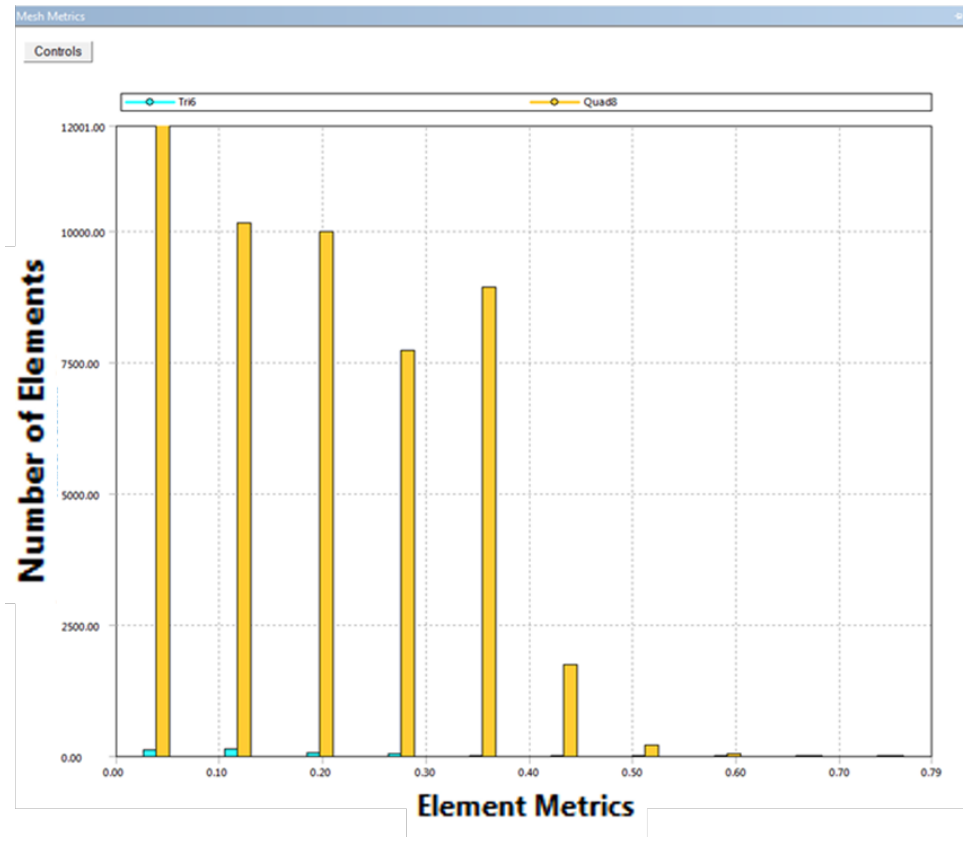

Figure 3 - 21: The skewness shows that the majority of the elements lie below 0.50 (good quality). All elements are considered acceptable.

Figure 3 - 22: All elements with skewness quality above 0.50.

CHAPTER 4: RESULTS AND DISCUSSION

All samples analyzed on the Instron testing systems were measure with a crosshead strain rate of 0.002 s^{-1}. Two bulk (Samples 1 and 2) and two AM (Samples 3 and 4) Ni-Mn-Ga samples were tested in uniaxial compression using the UVID system. Another three additively manufactured samples (Samples 5 to 7) were tested using the ARAMIS system. Stress was calculated from the load using $\sigma = P/A$. All samples were below the martensitic transformation finish temperature, so they should be purely in the martensitic phase.

4.1 Mechanical Properties of Ni-Mn-Ga Bulk Samples

Two Ni-Mn-Ga bulk samples (Sample 1 and Sample 2) were compression tested at Case Western Reserve University, and the strains were measured using UVID non-contact extensometer. As mentioned previously, three strain values (ε_1, ε_2, and ε_3) are found simultaneously using the UVID system. The positions of fiduciary points for measuring the strain values in the UVID system, for both bulk and AM samples, are shown in Figure 4-1 (a).

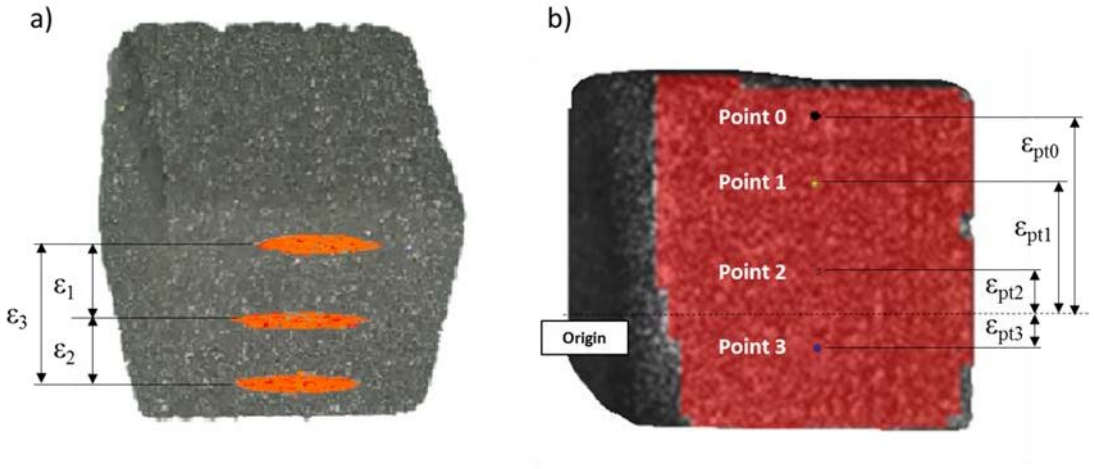

Figure 4 - 1: a) Locations of fiduciary points in UVID tested parts; b) Location of fiduciary points in ARAMIS tested parts.

In a homogenous, 100% dense sample, these strains should be nearly identical, but as can be seen in Figures 4-2 and 4-3, this is not the case.

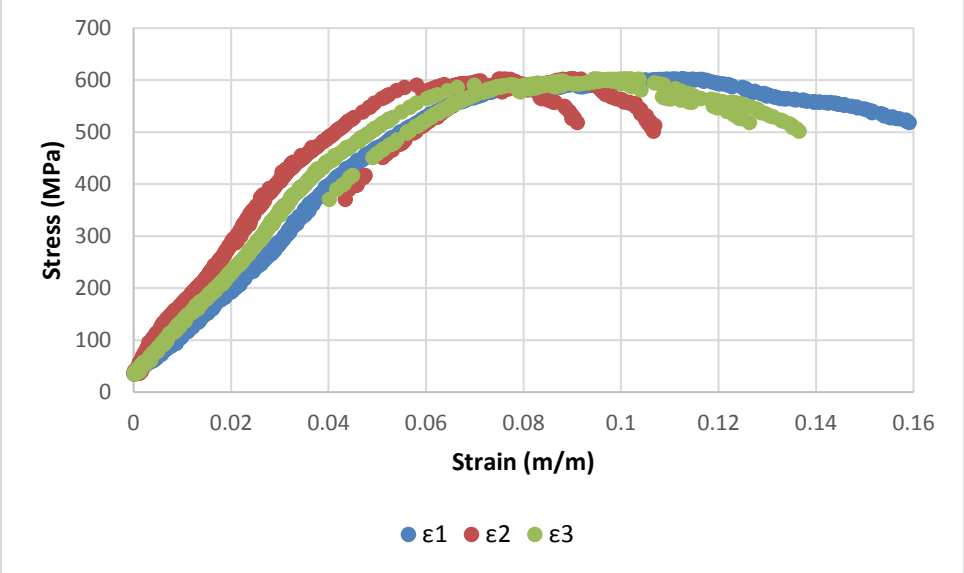

Figure 4 - 2: Uniaxial Compression of Bulk Polycrystalline Ni-Mn-Ga (Sample 1).

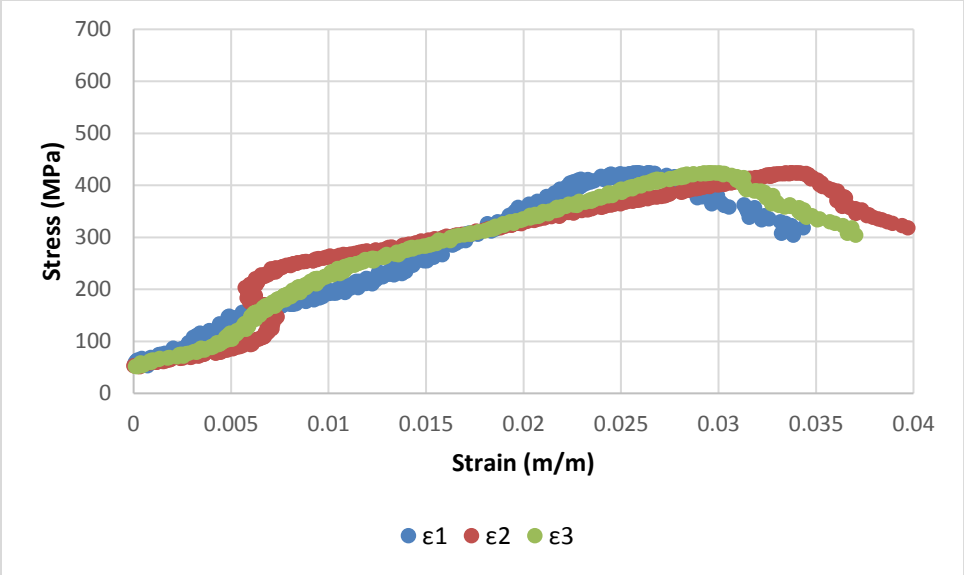

Figure 4 - 3: Uniaxial Compression of Bulk Polycrystalline Ni-Mn-Ga (Sample 2).

The reason for this heterogeneity in the bulk samples is not fully known, but a possible explanation is the uneven stress distribution within the samples as a result of the stress risers caused by unparallel faces. This might be related to the way the samples were shaped to size. These samples were cut using a diamond rotary blade, and upon visual inspection, one face was then manually polished to be near parallel with the other. It is possible, due to manual polishing, that the parallelism of the opposite faces might not be perfect. Also, martensite hardening might have happened on the polished surface, due to mechanical stresses developed during polishing. Unfortunately, no stress relief heat treatment was applied to the polished samples. Therefore, it had to be assumed that the induced stress from polishing the samples was localized at polished side. The uneven geometry combine with the existence of potential stress raisers in the samples, might explain the difference in compressive behavior between the two samples. In order to determine mechanical properties of the bulk samples, the two data sets were overlaid and the most similar stress-strain relationships were kept while the others were discarded.

For the two samples tested, ε_2 from Sample 1 and ε_1 from Sample 2 were overlapped, as shown in Figure 4-4.

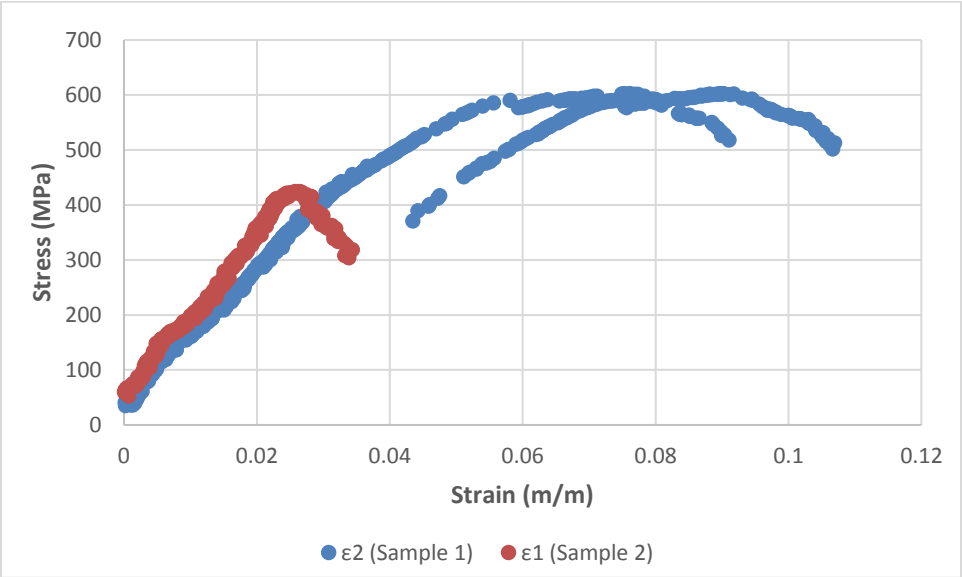

Figure 4 - 4: Overlapping of the compression curves corresponding to ε_2 from Sample 1 and ε_1 from Sample 2.

It may appear in Figure 4-4 that the ultimate stress of the Sample 1 is nearly twice that of the Sample 2. However, the independent stress-strain curve that compliments the main curve of Sample 1 above approximately 372 MPa is actually the result of a crack in the sample which split one of the fiduciary markers causing the UVID to read an additional data set. Removing the data beyond this fracturing point produces a stress-strain relationship much closer to that of the second sample. The data in Figure 4-5 is obtained by translating the curves in Figure 4-4 so that the slopes of the elastic regions pass through the origin. This makes acquiring the mechanical properties of the martensitic phase much easier.

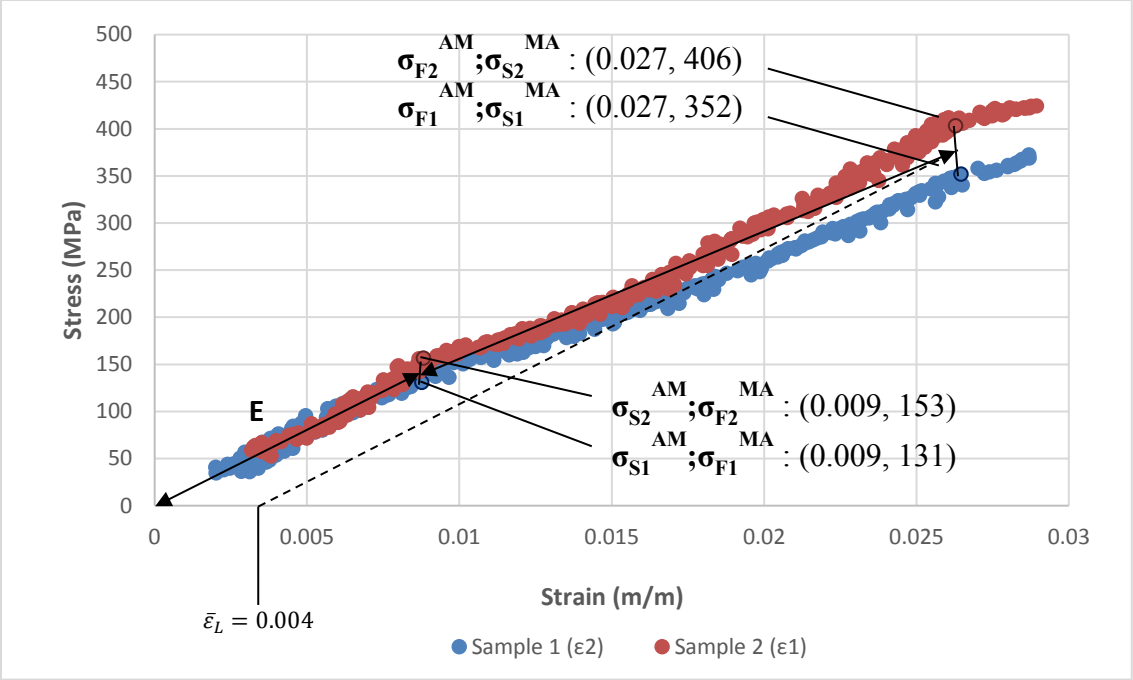

Figure 4 - 5: Mechanical Properties of Bulk Polycrystalline Martensitic Ni-Mn-Ga.

The inputs for the Engineering Data in ANSYS are for the *Isotriopy Elasticity* and *Superelasticity* options. Technically, because Sample 1 and Sample 2 were never in the austenite phase, during the compressive testing, they never displayed superelastic behavior. However, this feature is one that will be utilized in future work for modeling the transformation of Ni-Mn-Ga from austenite to martensite, so it was important to become familiar with it. In addition, this option was very accurate at capturing the hardening behavior of the material as unstressed martensite transitioned to stressed martensite, beginning at 0.009 m/m and ending at 0.027 m/m, Figure 4-5. Therefore, the mechanical properties of martensite in bulk polycrystalline Ni-Mn-Ga determined from the compressive behaviors in Figure 4-5 are presented below.

$$\boldsymbol{\sigma_s^{AM} = \sigma_f^{MA}} = \frac{(\boldsymbol{\sigma_s^{AM}})_1 + (\boldsymbol{\sigma_s^{AM}})_2}{2} = \frac{131\ MPa + 153\ MPa}{2} = \mathbf{142 \pm 11\ MPa}$$

$$\boldsymbol{\sigma_s^{MA} = \sigma_f^{AM}} = \frac{\left(\boldsymbol{\sigma_f^{AM}}\right)_1 + \left(\boldsymbol{\sigma_f^{AM}}\right)_2}{2} = \frac{372\ MPa + 424\ MPa}{2} = \mathbf{379 \pm 27\ MPa}$$

For the ultimate stress, the minimum value of the two samples (372 MPa) was used.

$$\boldsymbol{\sigma_{Ult} = 372\ MPa}$$

For the Young's modulus, a line of best fit was found for either sample using the respective data of their purely elastic regions (from ε = 0 to 0.009 m/m). The values found were E_1 = 15,744 MPa and E_2 = 17,426 MPa.

$$\boldsymbol{E} = \frac{E_1 + E_2}{2} = \frac{(15{,}744 + 17{,}426)}{2} = \mathbf{16{,}585 \pm 841\ MPa}$$

To find the value of the maximum residual strain ($\bar{\varepsilon}_L$) the following calculations were necessary.

$$\boldsymbol{\varepsilon_{Ult}} = \frac{\varepsilon_{Ult1} + \varepsilon_{Ult2}}{2} = \frac{0.027 + 0.027}{2} = \mathbf{0.027}$$

Maximum Residual Strain: $\sigma = E\varepsilon + \sigma_0$

$$\sigma - E\varepsilon = \sigma_0 \rightarrow (379\ MPa) - (16{,}585\ MPa)(0.027) = \textbf{-68.795 MPa}$$

$$\bar{\varepsilon}_L = \frac{\sigma - \sigma_0}{E} = \frac{0 - (-68.795\ MPa)}{16{,}585\ MPa} = \mathbf{0.004}$$

4.2 Mechanical Properties of AM Ni-Mn-Ga Samples

The mechanical properties of the AM Ni-Mn-Ga samples also showed quite large disparity. This can be seen in Figures 4-6 through 4-10. The plots in Figures 4-6 and 4-7 show the results obtained by compressive testing of AM Ni-Mn-Ga Sample 3 and Sample 4 using UVID system. Mechanical behavior of AM Ni-Mn-Ga Samples 5 to 7 have been obtained by using ARAMIS strain measurement system. The fiduciary points and corresponding strains in the case of the AM Ni-Mn-Ga samples tested in ARAMIS system are shown in Figure 4-1 (b).

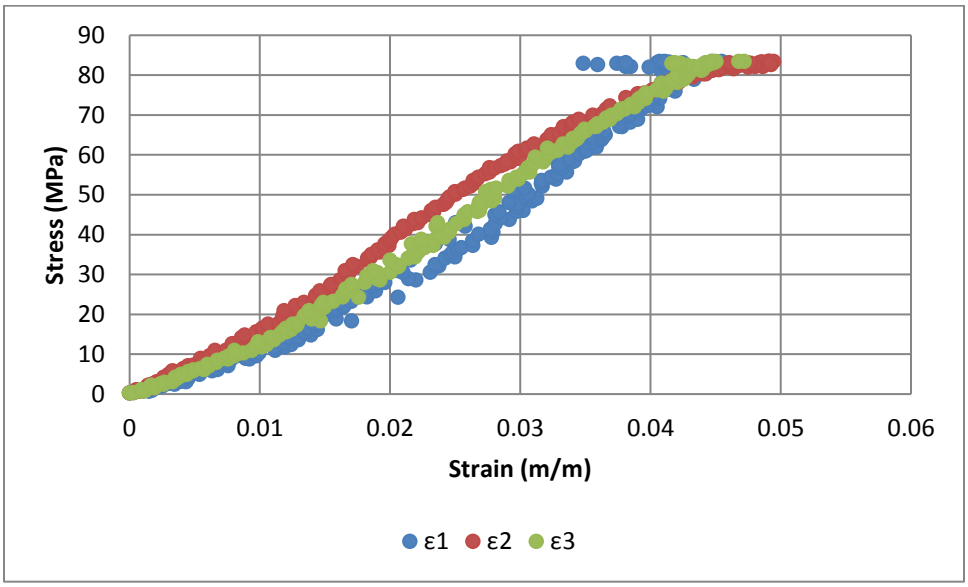

Figure 4 - 6: Mechanical behavior of uniaxial compressed AM Ni-Mn-Ga (Sample 3, UVID).

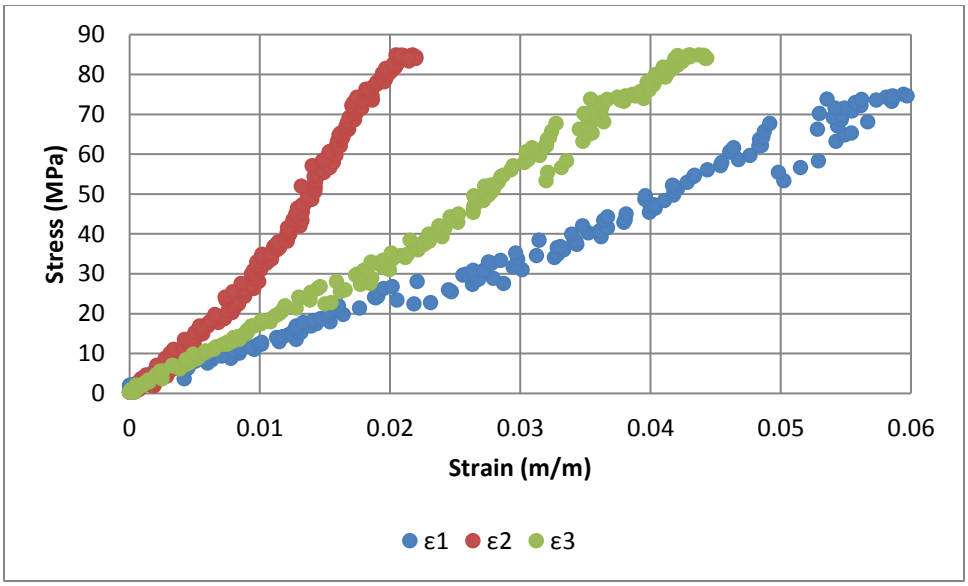

Figure 4 - 7: Mechanical behavior of uniaxial Compressed AM Ni-Mn-Ga (Sample 4, UVID).

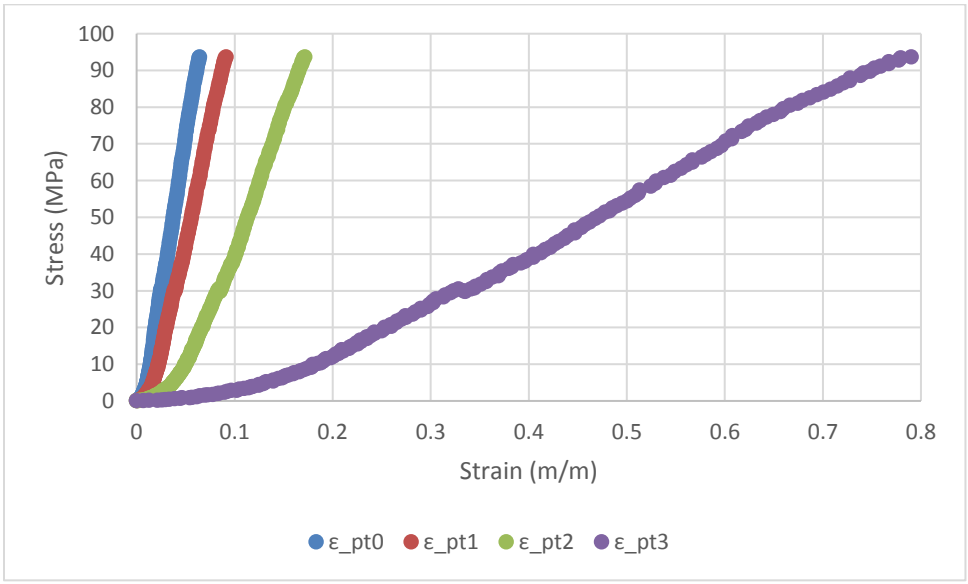

Figure 4 - 8: Mechanical behavior of uniaxial Compressed AM Ni-Mn-Ga (Sample 5; ARAMIS).

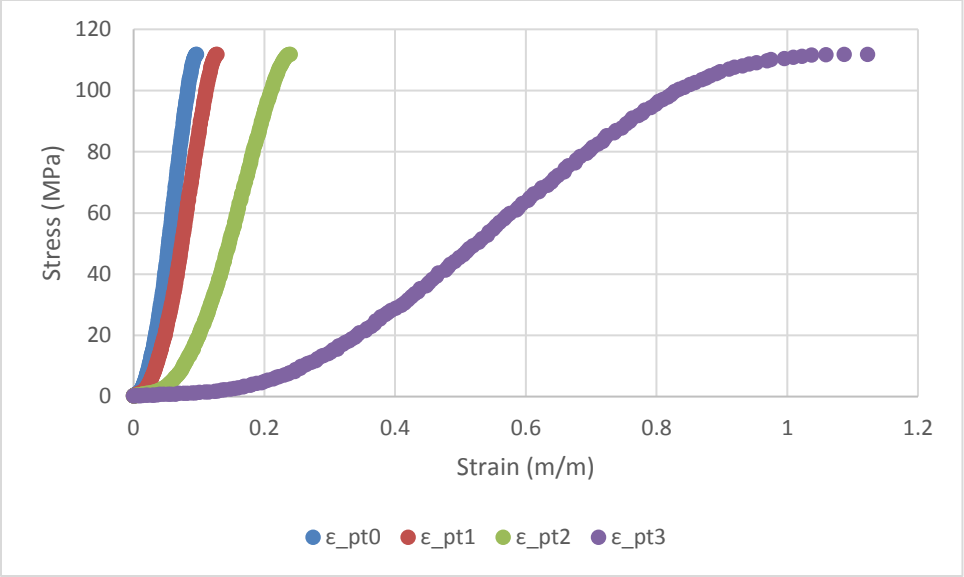

Figure 4 - 9: Mechanical behavior of uniaxial CompressedAM Ni-Mn-Ga (Sample 6; ARAMIS).

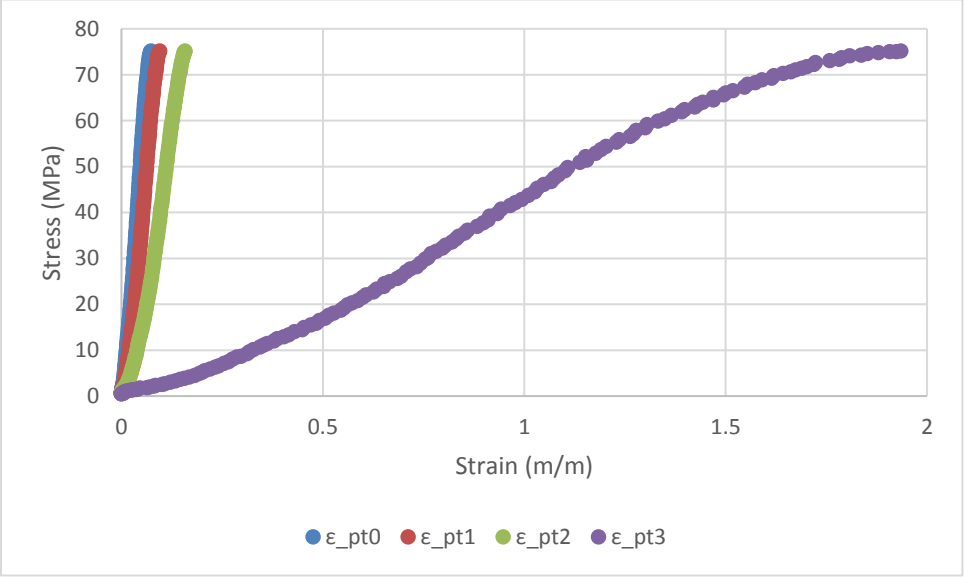

Figure 4 - 10: Mechanical behavior of uniaxial Compressed AM Ni-Mn-Ga (Sample 7; ARAMIS).

Upon inspection of Figures 4-6 through 4-10, it is clear that there is heterogeneity in the stress-strain distribution (localization) within AM parts. With the goal being to treat the AM parts as if they were a bulk material, more study is required on the stress-strain

behaviors of metallic foams to better interpret this data and to claim any correlations at large strain values. This localization is further realized after overlaying the data from all five AM samples (similar to what was done with the bulk samples), then keeping only one stress-strain curve per sample which corresponds closest with the others. The strains kept were ε_3 for the UVID tested AM samples and ε_{pt0} for the ARAMIS tested AM samples, as shown in Figure 4-11. With the closest matching stress-strain behaviors being so dissimilar, it becomes even clearer that a different means of analysis is required if reliable mechanical properties are to be concluded from this data.

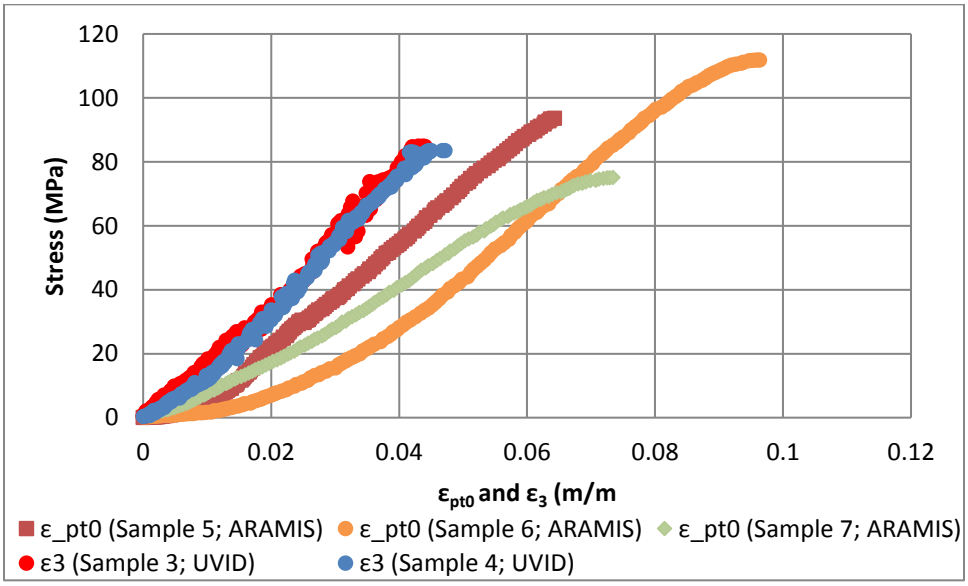

Figure 4 - 11: Experimental uniaxial compression of AM Ni-Mn-Ga. Five plots corresponding to five individual strain measurements have been plotted together for comparison.

The causes of the heterogeneity in the AM samples are likely the same as those for metallic foams. As mentioned before, AM parts resemble structures more than they do bulk materials. This means stress and strain in the part are not uniform. Stress risers occur in the pores at edges where particles are connected. Localized deformation occurs

when the material fails at these stress risers, and the pores collapse in on themselves. These localized deformations then link, forming deformation bands which are typically normal to the applied stress. These normal planes are the weakest regions of the sample for a couple of reasons. One is because lateral strain in AM bodies and metallic foams is negligible compared to the longitudinal strains. Another reason is due to inhomogeneity of the plane's density (or density of the 3D print layer in the case of AM bodies). When one layer fails, the stress distribution becomes even more uneven which causes layers adjacent to it to also fail[36]. Another potential cause of the localization in these samples is again unparallel surfaces. The AM samples were not cut or polished like the bulk samples, but surfaces are sometimes slightly distorted during the sintering process. These deformation bands, as well as a stress riser due to unparallel surfaces, can be seen in Figure 4-12.

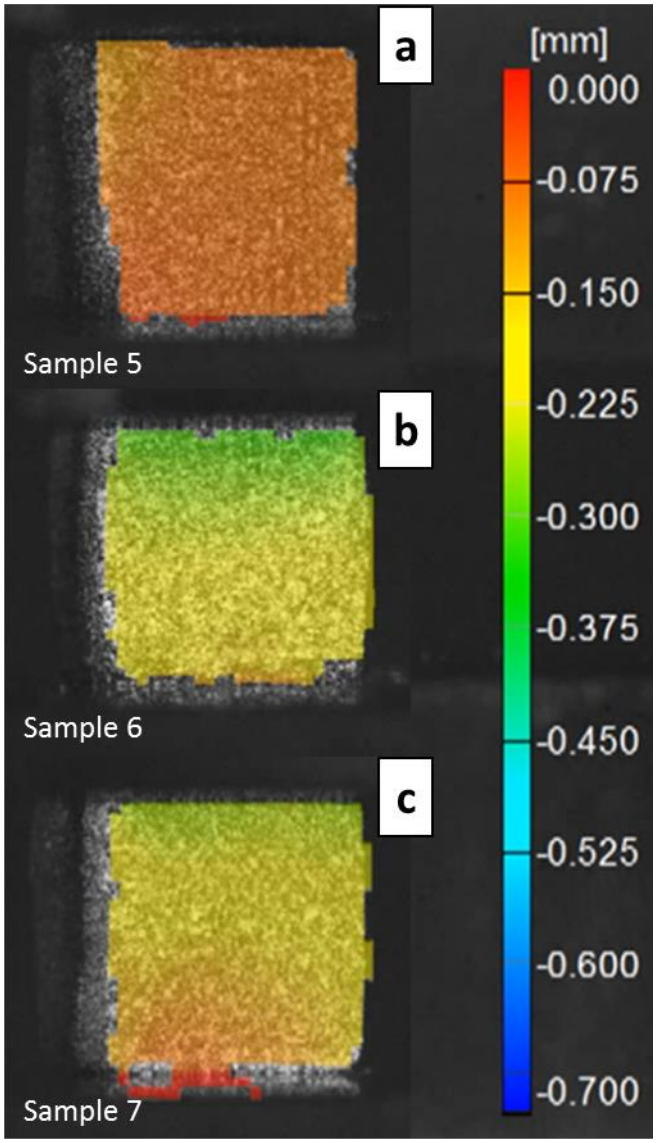

Figure 4 - 12: Deformation gradient in AM Samples 5, 6, and 7: a) Noticeable stress riser at the top left corner of Sample 5 from uneven load surface; b) Noticeable deformation band at top of Sample 6; c) Noticeable deformation band at the top of Sample 7.

Samples 5, 6, and 7 shown in Figure 4-12 are being compressed from the top. The heterogeneity of the color schemes are visualizations of the localized deformations. Though this behavior of porous metals is well documented in literature, few papers present models that can simulate, and accurately predict it.

4.3 Modeling of mechanical behavior of AM Ni-Mn-Ga

For this work, each 2D model was 360 µm tall and 480 µm wide. First the model was analyzed to see its ability to predict large strains in the AM part. Then it was used to determine the part's fully elastic deformation limit (small strains), or rather the strain magnitude at which material failure at the stress risers begins. In theory, AM parts should behave similarly to bulk materials in these regions of small strains, and accurate mechanical properties could potentially be assigned to them. The maximum loading stress applied to the AM sample model is shown in Figure 4-13.

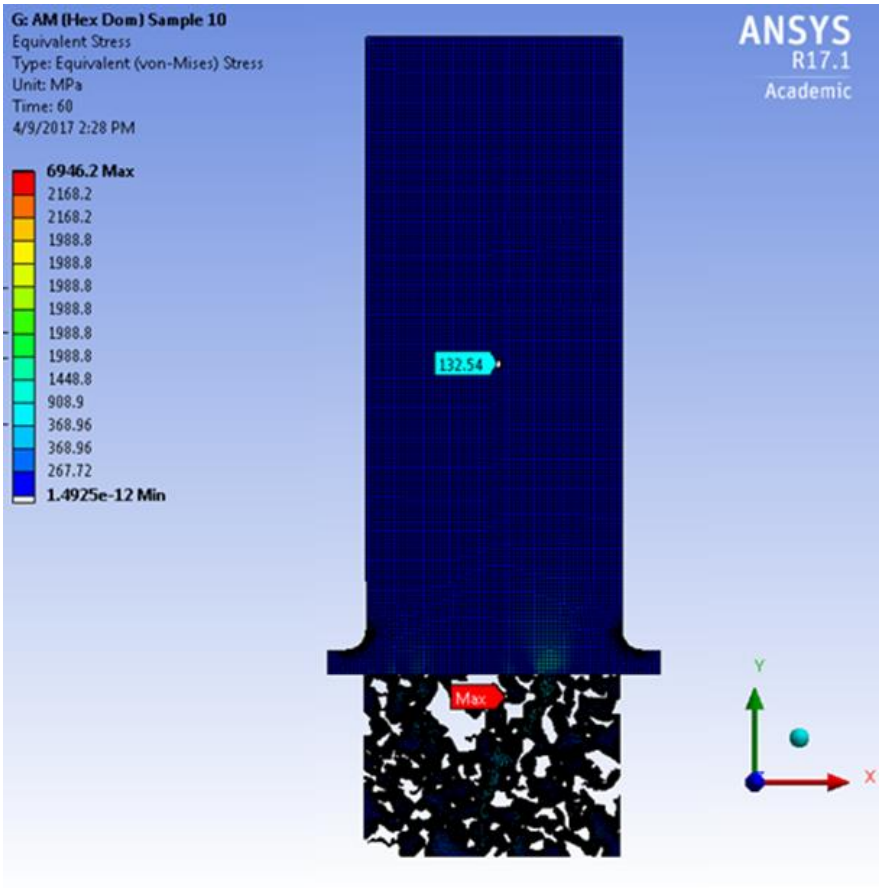

Figure 4 - 13: Max loading stress on the AM sample.

Figure 4-14 shows the ANSYS model's results for large strain compared to the experimental data for strains ε_{pt0} and ε_3.

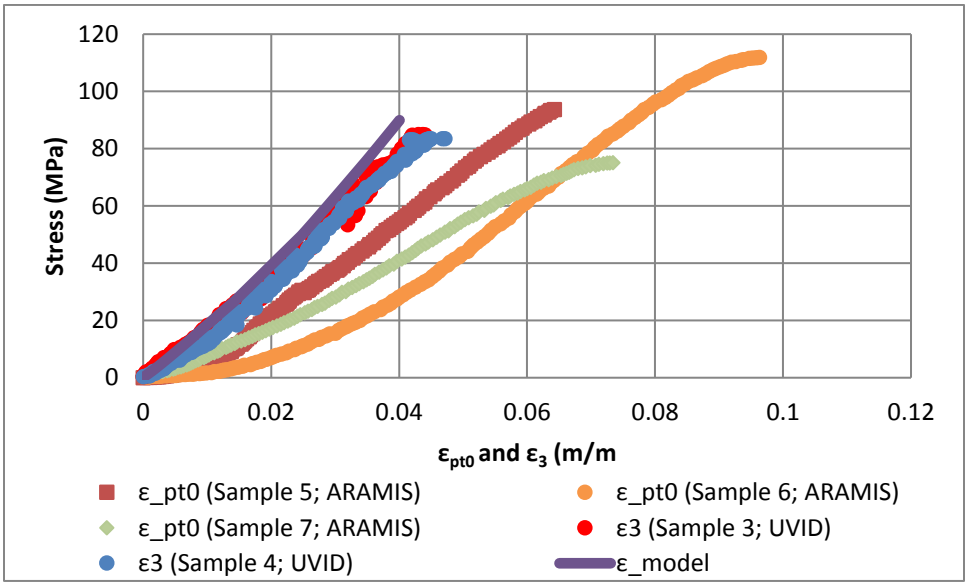

Figure 4 - 14: ANSYS model's prediction of large compressive strains compared with experimental uniaxial compression of AM Ni-Mn-Ga

Relating Figures 4-12 through 4-14, it would appear that as the vertical measurement range approaches the full height of the sample (L_0), the steeper the slope of the stress-strain relationships, and the more similar they become to one another. For instance, the stress-strain behavior of ε_3 and ε_{model} are very similar in Figure 4-14, and so too are the vertical ranges they were measured from, Figure 4-15. The measured range of ε_{pt0} is slightly less than ε_3, and responsively the slope stress-strain behavior is also less. The relationship between the heights of the strain measurement ranges and the slopes of their respective stress-strain curves is consistent for all AM samples tested. This can be seen by analyzing stress-strain plots in Figures 4-6 through 4-10 in relation with strain measurement schemes in Figures 4-1 and 4-15.

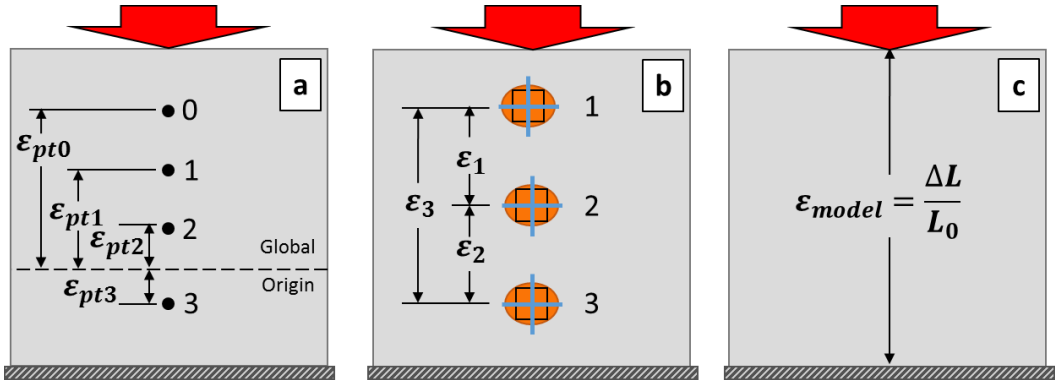

Figure 4 - 15: Strain measurement ranges: (a) ARAMIS system; (b) UVID system; (c) ANSYS model.

Figure 4-16 shows the stress distribution in the printed Ni-Mn-Ga part. The largest six stress risers can also be seen in the figure and are denoted 1 to 6. Details of each of the six selected stress risers are shown in Figure 4-17.

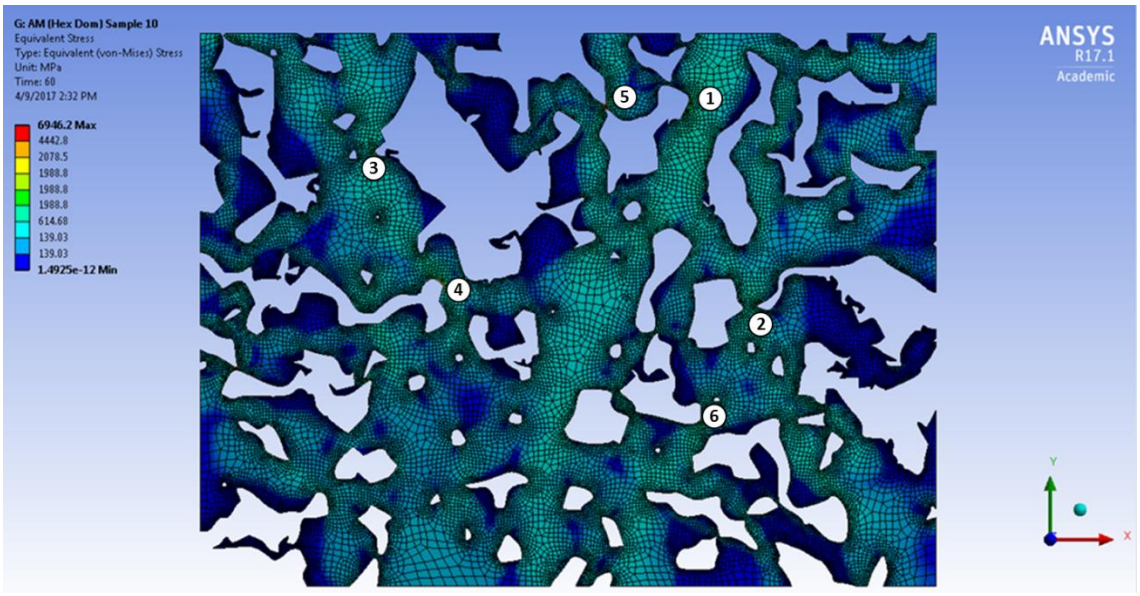

Figure 4 - 16: Stress distribution in the AM part and largest six stress risers.

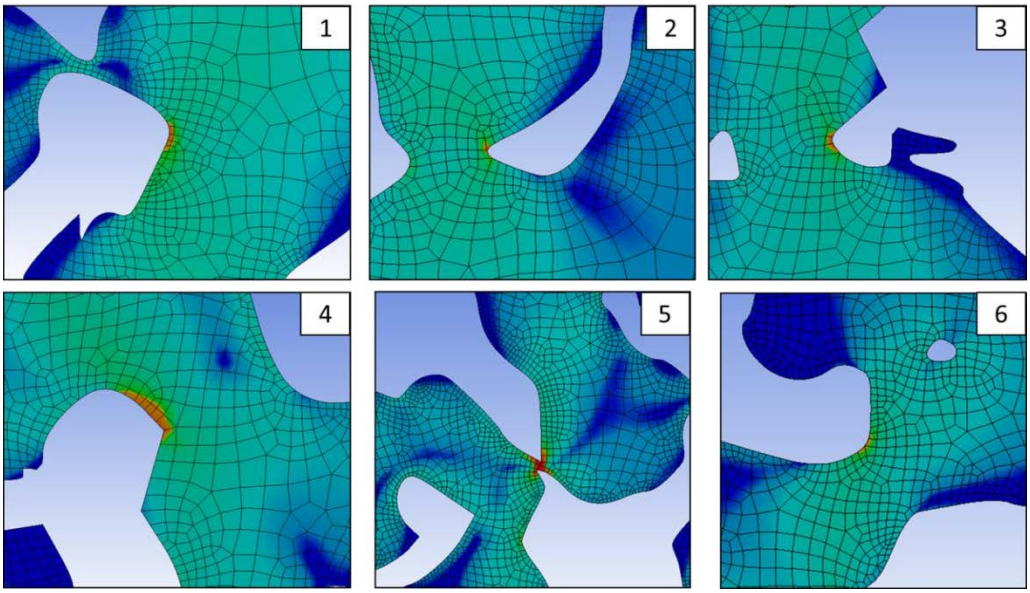

Figure 4 - 17: Detail of highest stress risers in Figure 4-16.

Once again, it should be addressed that without a convergence test proving the mesh, all of these values at the stress risers might slightly be inaccurate. This being said, the average stress value taken at these locations was recorded, and it was found that at a deformation of 1.770 μm failure began to occur. This deformation was then used to interpret yield strain for AM Ni-Mn-Ga of ε_y = 0.0049 m/m. This and the yield stress associated to it (σ_y = 8.72 MPa) is shown in Table 4-1. If this model is accurate, this strain should correspond to some noticeable change in the stress-strain behavior of the experimental data as strain in the part transitions from elastic to plastic strain.

Table 4 - 1: Maximum stress and recoverable strain of AM part.

FEA of SEM Based Additively Manufactured Geometry										
Deformation of Crosshead (μm)	Stress (Mpa)	Stress (Mpa)	Stress (Mpa)	Stress (Mpa)	Stress (Mpa)	Stress (Mpa)	Stress (Mpa)	Standard Deviation (Mpa)	Strain	Stress (Mpa)
	Point 1	Point 2	Point 3	Point 4	Point 5	Point 6	Average		Part	Part
0.000	4.737	14.137	5.865	3.916	7.404	14.603	8.443517	4.326762	0.0000	0.1390
0.033	9.477	28.278	11.731	7.832	14.810	29.210	16.88978	8.654471	0.0001	0.2781
0.067	14.249	42.459	17.610	11.755	22.243	43.860	25.363	12.9933	0.0002	0.4178
0.100	19.073	56.710	23.512	15.690	29.721	58.584	33.882	17.35133	0.0003	0.5585
...	...	...	...	...	...	...	...	...	...	...
1.770	260.860	626.940	240.980	214.960	285.920	626.940	376.100	178.6419	0.0049	8.7287

The fully elastic region of the model is shown in Figure 4-18.

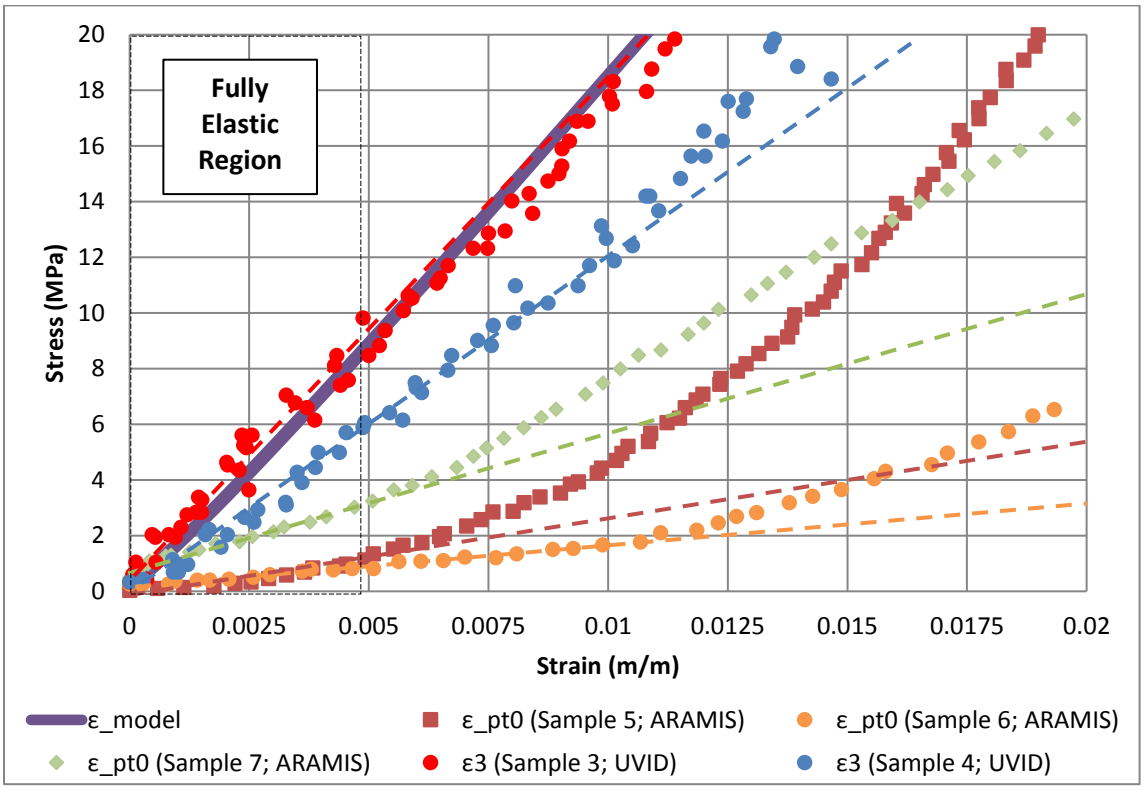

Figure 4 - 18: Fully elastic region of AM part (ε_{model}, ε_{pt3} and ε_3).

Figure 4-18 shows ε_3 and ε_{pt0} as dots. The dashed lines correspond to the average trend of the data up until the strain is equal to 0.0049. Interestingly, for all three ARAMIS

tested samples as well as Sample 2 tested with the UVID system, there appears to be a deviation of the data at this particular strain. In addition, the same approach was used to see if an elastic region was apparent in the strain range of the other extreme (ε_{pt0}). This is shown below in Figure 4-19.

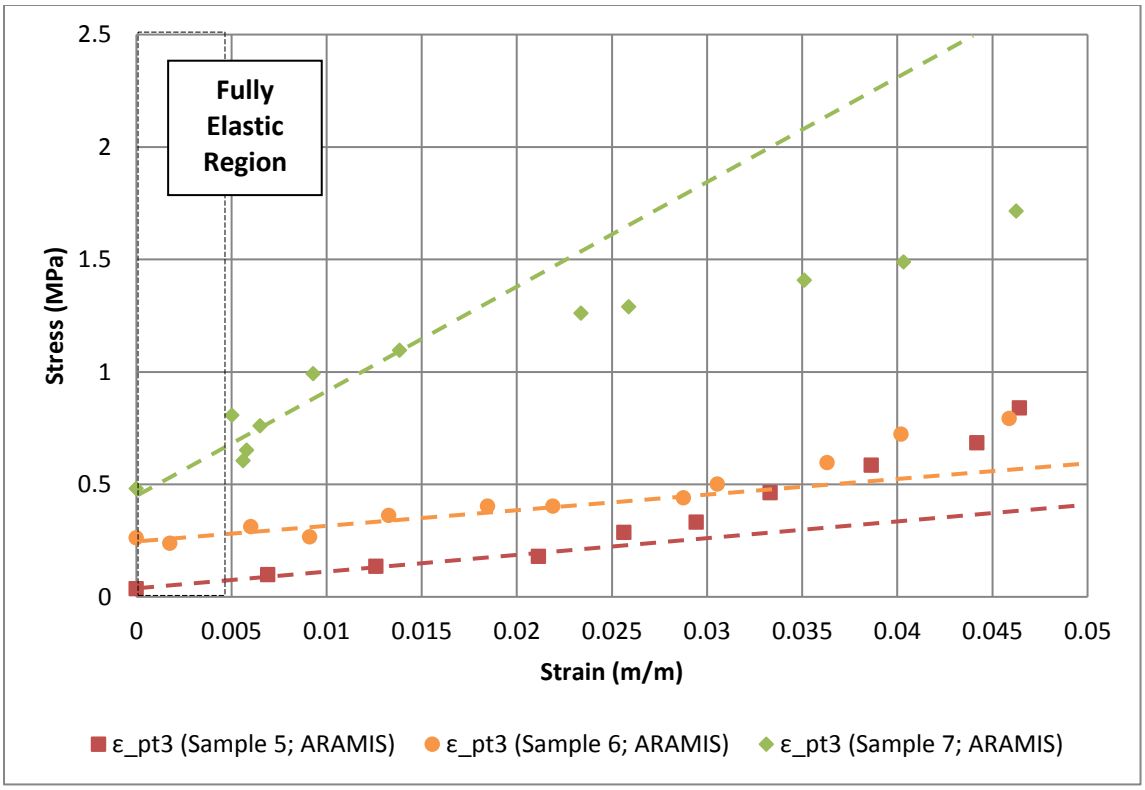

Figure 4 - 19: Fully elastic region of AM part (ε_{pt0}).

Figure 4-19 also shows deviation of the stress-strain curve around 0.0049 m/m. This gives a measure of legitimacy to the model. If the model is correct, the stress-strain relationship of the AM Ni-Mn-Ga samples is fully elastic and recoverable within this range, and mechanical properties can be associated with it. In other words, the AM sample is behaving similarly to a bulk material. As exciting as this claim could be there simply isn't enough data yet to support it officially, so for now, no mechanical properties

are being claimed. The mesh first would needs proven through a convergence test, many more models are required, and more AM sample need to be tested experimentally showing the exact same trend increase the population size of the data and confirm accuracy of this modeling technique.

CHAPTER 5: CONCLUSIONS AND FUTURE WORK

5.1 Conclusions

Additively manufacturing FSMAs might benefit their magnetic field induced strain and allow for the manufacturing of much more complicated parts, but this process has several drawbacks. The porous nature of AM parts can make them unpredictable, as stress, strain, and likely magnetic flux, are not distributed through them uniformly. In the case of metallic foams, it has been proposed that bulk mechanical properties can be given to them and they can be treated as a new material. However, rigorous testing and a surplus of experimental data are typically required to assign these mechanical properties with any real degree of certainty. With limited access to proper instrumentation, an attempt was made to predict mechanical properties of additively manufactured Ni-Mn-Ga using finite element analysis and a SEM micrograph-based geometry from the cross section of an AM part. First, bulk and AM Ni-Mn-Ga samples were tested in compression using digital image correlation as strain measuring technique. This technique proved invaluable for this experiment as the samples tested were small and heterogeneous. An AM part was then modeled using the material properties of bulk polycrystalline Ni-Mn-Ga. The mechanical properties of the bulk material is shown below in Table 5.1.

Table 5 - 1: Properties of bulk and AM polycrystalline Ni-Mn-Ga (martensitic)

	E (Mpa)	σ_s^{AM} (Mpa)	σ_f^{AM} (Mpa)	σ_s^{MA} (Mpa)	σ_f^{MA} (Mpa)	$\bar{\varepsilon}_L$
Bulk	16585 ± 841	142 ± 11	379 ± 27	142 ± 11	379 ± 27	0.00366

Strain was calculated in the ANSYS model using the displacement of the crosshead of the compressor divided by the original height of the sample. Stress was calculated at a region of the compressor of the same width as the part and a characteristic length away from the compressor-part interface. For AM parts, mechanical property measurements must take into account the porosity's influence. To do this, six points in the model showing the greatest stress concentrations were tracked and the displacement of the crosshead associated to failure at these stress risers was determined. This displacement is associated to a maximum elastic strain of 0.0049 m/m for the AM model. Experimental data backs a linear relationship of the stress-strain behaviors of the parts up until this strain. Therefore, it would appear that for small stresses and strains, this modeling technique can potentially be used for describing mechanical properties of AM parts.

5.2 Future Work

In the future, more samples (bulk and AM) should be experimentally tested to better understand their mechanical properties and behaviors. More models should also be run since a single model is not sufficient enough of a representation of the entire sample. These models must then undergo convergence testing to prove their accuracy. With more data, both experimental and modeling, it may be possible to calculate an effective Young's modulus describing the stress-strain relationship of the fully elastic region, as well as other mechanical properties. This modeling technique should also be used with bulk properties of Ni-Mn-Ga in the austenitic phase to see how well the SEM-based geometry represents the shape memory effect of the AM parts. In addition, the 2D model must be refined and pass a convergence test to ensure its accuracy. This may require a higher ANSYS license, and possibly a more powerful computer to produce a fine mesh with sufficient elements around the stress risers. Also, more research should be done into metallic foams and how literature derives justifiable mechanical properties for heterogeneous bodies to confirm results found by modeling. Lastly, is would prove useful to expand this 2D numerical model into a 3D model to even better simulate the AM Ni-Mn-Ga.

CHAPTER 6: REFERENCES

[1] Lorenza Petrini et al., "Computational Studies of Shape Memory Alloy Behavior in Biomedical Applications," *Journal of Biomechanical Engineering* 127, no. 4 (2005): 716, doi:10.1115/1.1934203.

[2] Sonia Degeratu et al., "Thermal Study of a Shape Memory Alloy (SMA) Spring Actuator Designed to Insure the Motion of a Barrier Structure," *Journal of Thermal Analysis and Calorimetry* 111, no. 2 (February 2013): 1255–62, doi:10.1007/s10973-012-2369-4.

[3] Ferdinando Auricchio et al., "A Phenomenological Model for the Magneto-Mechanical Response of Single-Crystal Magnetic Shape Memory Alloys," *European Journal of Mechanics - A/Solids* 52 (July 2015): 1–11, doi:10.1016/j.euromechsol.2014.12.011.

[4] Lorenza Petrini et al., "Computational Studies of Shape Memory Alloy Behavior in Biomedical Applications," *Journal of Biomechanical Engineering* 127, no. 4 (2005): 716–25, doi:10.1115/1.1934203.

[5] Yong Liu, "Laboratory of Smart Materials and Structures," January 23, 2017, http://www.ntu.edu.sg/home/mliuy/New%20files/SMS%20Lab.htm.

[6] H. Tan and M. H. Elahinia, "On the Modeling of Ferromagnetic Shape Memory Alloy Actuators" (WORLD SCIENTIFIC, 2006), 442–53, doi:10.1142/9789812772428_0051.

[7] Susanne Glock et al., "Magneto-Mechanical Actuation of Ferromagnetic Shape Memory Alloy/Epoxy Composites," *Composites Science and Technology* 114 (June 2015): 110–18, doi:10.1016/j.compscitech.2015.04.009.

[8] A. Hubert et al., "Magnetic Shape Memory Alloys as Smart Materials for Micro-Positioning Devices," *Advanced Electromagnetics* 1, no. 2 (August 2012): 75–84.

[9] B. Kiefer and D. C. Lagoudas, "Modeling of Magnetic SMAs," in *Shape Memory Alloys*, vol. 1 (Boston, MA: Springer US, 2008), 325–93, http://link.springer.com/10.1007/978-0-387-47685-8_7.

[10] K. Bhattacharya, *Microstructure of Martensite: Why It Forms and How It Gives Rise to the Shape-Memory Effect*, Oxford Series on Materials Modelling 2 (Oxford ; New York: Oxford University Press, 2003).

[11] A. Stebner et al., "Development, Characterization, and Design Considerations of Ni19.5Ti50.5 Pd25Pt5 High-Temperature Shape Memory Alloy Helical Actuators," *Journal of Intelligent Material Systems and Structures* 20, no. 17 (November 1, 2009): 2107–26, doi:10.1177/1045389X09347018.

[12] A. Kumar, "Comprehensive Modeling of Shape Memory Alloys for Actuation of Large-Scale Structures" (Doctor of Philosophy, University of Akron, 2010).

[13] *ANSYS Workbench Help // ANSYS Documentation // Mechanical APDL // Technology Demonstration Guide // 40 Shape Memory Alloy (SMA) with Thermal Effect*, version 17.1, Workbench (ANSYS Inc., 2016).

[14] K.V. Redkin et al., "Microscale Image-Based Finite Element Modeling of High Speed Steel Microstructure" (WHEMCO Inc., Product Developement, n.d.).

[15] "OOF: Finite Element Analysis of Microstructures," accessed April 29, 2017, http://www.ctcms.nist.gov/oof/.

[16] S. Roth et al., "Magneto-Mechanical Behaviour of Textured Polycrystals of NiMnGa Ferromagnetic Shape Memory Alloys," *Advanced Materials Research* 52 (2008): 29–34, doi:10.4028/www.scientific.net/AMR.52.29.

[17] Jian Liu et al., "NiMn-Based Alloys and Composites for Magnetically Controlled Dampers and Actuators," *Advanced Engineering Materials* 14, no. 8 (August 2012): 653–67, doi:10.1002/adem.201200038.

[18] P. Müllner et al., "Large Cyclic Magnetic-Field-Induced Deformation in Orthorhombic (14M) Ni–Mn–Ga Martensite," *Journal of Applied Physics* 95, no. 3 (February 2004): 1531–36, doi:10.1063/1.1639144.

[19] N. Scheerbaum et al., "Textured Polymer Bonded Composites with Ni–Mn–Ga Magnetic Shape Memory Particles," *Acta Materialia* 55, no. 8 (May 2007): 2707–13, doi:10.1016/j.actamat.2006.12.008.

[20] P. Müllner et al., "Recent Developments in Ni-Mn-Ga Foam Research," *Materials Science Forum* 635 (December 2009): 119–24, doi:10.4028/www.scientific.net/MSF.635.119.

[21] D.C. Jiles, "Recent Advances and Future Directions in Magnetic Materials," *Acta Materialia* 51, no. 19 (November 2003): 5907–39, doi:10.1016/j.actamat.2003.08.011.

[22] M.P. Caputo and C.V. Solomon, "A Facile Method for Producing Porous Parts with Complex Geometries from Ferromagnetic Ni-Mn-Ga Shape Memory Alloys," *Materials Letters*, April 2017, doi:10.1016/j.matlet.2017.04.112.

[23] M.P. Caputo et al., "Electron Microscopy Investigation of Binder Saturation and Microstructural Defects in Functional Parts Made by Additive Manufacturing,"

Microscopy and Microanalysis 22, no. S3 (July 2016): 1770–71, doi:10.1017/S1431927616009697.

[24] R.J. Budynas, *Advanced Strength and Applied Stress Analysis*, 2nd ed. (McGraw Hill Publishing Company, 1999).

[25] Correlated Solutions, Inc., "Digital Image Correlation: Overview of Principles and Software" (SEM 2009 Workshop, University of South Carolina, 2009), https://www.researchgate.net/file.PostFileLoader.html?id=54abf43ad039b1e37f8b45aa&assetKey=AS%3A273664212176896%401442258040146.

[26] "Arion 1-D Axial Measurement System" (UVID Enterprises, LLC, n.d.), www.uvid-llc.com.

[27] "Digital Image Correlation," accessed April 5, 2017, http://gr.xjtu.edu.cn/web/liangjin/9.

[28] C.A. Felippa, "Review of Continuum Mechanics: Field Equations," in *Nonlinear Finite Element Methods*, NFEM (Department of Aerospace Engineering Sciences and Center for Space Structures and Controls University of Colorado, 2001), Chapter 8, http://www.colorado.edu/engineering/cas/courses.d/NFEM.d/NFEM.Ch07.d/NFEM.Ch07.pdf.

[29] J.M. Hein, *Ultrasonic and Stereo-Optical Characterization Techniques for Applications in Mechanical Testing*, 2011, http://digitalcommons.unl.edu/cgi/viewcontent.cgi?article=1019&context=engmechdiss.

[30] J. Čapek et al., "Microstructural and Mechanical Properties of Biodegradable Iron Foam Prepared by Powder Metallurgy," *Materials & Design* 83 (October 2015): 468–82, doi:10.1016/j.matdes.2015.06.022.

[31] E. Hernández-Nava et al., "The Effect of Density and Feature Size on Mechanical Properties of Isostructural Metallic Foams Produced by Additive Manufacturing," *Acta Materialia* 85 (February 2015): 387–95, doi:10.1016/j.actamat.2014.10.058.

[32] A. Brothers and D. Dunand, "Plasticity and Damage in Cellular Amorphous Metals," *Acta Materialia* 53, no. 16 (September 2005): 4427–40, doi:10.1016/j.actamat.2005.06.002.

[33] "Convertio," n.d., https://convertio.co/.

[34] P. Lethbridge, "An Overview of ANSYS Acedemic Products and Release 11.0," June 9, 2008, http://www.ozeninc.com/downloads/academic_article_pdf_1.pdf.

[35] M. Ozen, Ph.D, "Meshing Workshop," November 13, 2014.

[37] C.M. Cady et al., "Compressive Properties of a Closed-Cell Aluminum Foam as a Function of Strain Rate and Temperature," *Materials Science and Engineering: A* 525, no. 1–2 (November 2009): 1–6, doi:10.1016/j.msea.2009.07.007.